

The opaque nascent starburst in NGC 1377: Spitzer SINGS observations

H. Roussel^{1,2}, G. Helou¹, J.D. Smith³, B.T. Draine⁴, D.J. Hollenbach⁵, J. Moustakas³, H.W. Spoon⁶, R.C. Kennicutt^{7,3}, G.H. Rieke³, F. Walter², L. Armus¹, D.A. Dale⁸, K. Sheth¹, G.J. Bendo⁹, C.W. Engelbracht³, K.D. Gordon³, M.J. Meyer¹⁰, M.W. Regan¹⁰, E.J. Murphy¹¹

1) *California Institute of Technology, Pasadena, CA 91125*

2) *Max-Planck-Institut für Astronomie, Heidelberg, 69117 Germany*

3) *Steward Observatory, University of Arizona, Tucson, AZ 85721*

4) *Princeton University, Princeton, NJ 08544*

5) *NASA Ames Research Center, Moffett Field, CA 94035*

6) *Cornell University, Ithaca, NY 14853*

7) *IoA, University of Cambridge, UK*

8) *University of Wyoming, Laramie, WY 82071*

9) *Imperial College, London SW7 2AZ, UK*

10) *Space Telescope Science Institute, Baltimore, MD21218*

11) *Yale University, New Haven, CT 06520*

roussel@mpia-hd.mpg.de

ABSTRACT

We analyze extensive data on NGC 1377 from the Spitzer Infrared Nearby Galaxies Survey (SINGS). Within the category of nascent starbursts, that we previously selected as having infrared to radio continuum ratios in large excess of the average, and containing hot dust, NGC 1377 has the largest infrared excess yet measured. Optical imaging reveals a morphological distortion suggestive of a recent accretion event. Infrared spectroscopy reveals a compact and opaque source dominated by a hot, self-absorbed continuum ($\tau \sim 20$ in the $10 \mu\text{m}$ silicate band). We provide physical evidence against non-stellar activity being the heating source. HII regions are detected through the single [NeII] line, probing

< 1% of the ionizing radiation. Not only is the optical depth in different gas and dust phases very high, but > 85% of ionizing photons are suppressed by dust. The only other detected emission features are molecular hydrogen lines, arguably excited mainly by shocks, besides photodissociation regions, and weak aromatic bands. The new observations support our interpretation in terms of an extremely young starburst (< 1 Myr). More generally, galaxies deficient in radio synchrotron are likely observed within a few Myr of the onset of a starburst and after a long quiescence, prior to the replenishment of the interstellar medium with cosmic rays. The similar infrared-radio properties of NGC 1377 and some infrared-luminous galaxies suggest that NGC 1377 constitutes an archetype to better understand starburst evolution. Although rare locally because observed in a brief evolutionary stage, nascent starbursts may represent a non-negligible fraction of merger-induced starbursts dominating deep infrared counts. Since they differ dramatically from usual starburst templates, they bear important consequences for the interpretation of deep surveys.

Subject headings: dust, extinction — galaxies: individual (NGC 1377) — galaxies: ISM — galaxies: starburst — galaxies: evolution — infrared: galaxies

1. Introduction

The infrared-radio correlation of star-forming galaxies (Helou et al. 1985; de Jong et al. 1985) suffers very few exceptions. At centimeter wavelengths, the radio continuum of massive galaxies is dominated by synchrotron emission, from cosmic ray electrons previously accelerated in type-II supernova remnants, propagating in the interstellar magnetic field, and decaying in less than 10^8 years (Condon 1992). The emission from thermal electrons in HII regions usually contributes only of the order of 20% of the total emission of galaxies at 3 cm, and of the order of 5% at 20 cm. The far-infrared continuum measures the energy peak of the dust emission, and is a fair tracer of the instantaneous star formation rate for dusty starburst galaxies. In more quiescent galaxies, a significant fraction of the far-infrared emission can originate from dust heated by intermediate-mass stars (Lonsdale-Persson & Helou 1987; Sauvage & Thuan 1992).

NGC 1377 is the most extreme example known so far of the rare category of non-dwarf galaxies which have infrared-to-radio ratios in significant excess of the average, and where the infrared excess is not attributable to cirrus-like emission ; this is because the high dust temperatures of the selected galaxies imply high radiation field intensities (Roussel et al. 2003, 2005). In NGC 1377, synchrotron emission is deficient by at least a factor 37 (i.e. by

$> 8\sigma$) with respect to normal galaxies. In addition, HII regions were not detected through near-infrared hydrogen recombination lines nor through the thermal radio continuum, and the upper limits that we obtained imply that they are fainter than expected for normal starbursts by at least 70%, likely due to the fact that most ionizing photons are absorbed by dust.

The infrared and radio emission both have their source in the star formation activity. Given the lack of direct connection between the physical processes regulating both types of emission, however, the infrared-radio correlation can hold only if strong coupling mechanisms operate (Beck & Golla 1988; Helou & Bicay 1993; Niklas & Beck 1997). First, the production rate of cosmic rays has to be roughly proportional to that of dust-heating photons (which is achieved for a constant initial mass function). In addition, the magnetic field intensity has to be coupled with either the gas density or the star formation rate (e.g. turbulence driven by massive star formation inducing rapid amplification of the magnetic field). Empirically, starbursts seem to constantly adjust their magnetic field so that the ratio of magnetic energy density to radiation energy density remains constant, including ultraluminous galaxies with very intense radiation fields (Condon et al. 1991; Lisenfeld et al. 1996).

The infrared emission and the radio continuum both persist for long periods subsequent to an instantaneous episode of star formation, but follow very different timescales. In particular, cosmic rays are accelerated only about 4 Myr after the birth of massive stars evolving into type-II supernovae, whereas dust is heated almost instantaneously. This time delay implies that the relative amounts of infrared and radio emission are expected to vary significantly, which can in principle be exploited to constrain the age of individual star forming regions, i.e. regions with relatively simple star formation histories. Galaxies, however, host young stellar populations which span an extended age range, and star formation generally goes on for long periods, either continuously or in the form of recurrent bursts. For large regions within galaxies, systematic variations of the infrared-to-radio ratio are thus in practice erased by complex star formation histories. Non-uniform interstellar medium properties (structure and dust content) will also induce further variations decoupled from age.

Discrete sources with radio spectra dominated by optically-thick thermal emission, from ultracompact HII regions, have been found and studied at high angular resolution within starbursting galaxies, most of them dwarfs: e.g. by Turner et al. (1998) in NGC 5253, Kobulnicky & Johnson (1999) in He 2-10, Tarchi et al. (2000) in NGC 2146, Beck et al. (2000) in several Wolf-Rayet galaxies, Beck et al. (2002) in II Zw 40. These systems thus contain a number of very young star forming sites. On global scales, the radio continuum of blue compact dwarf galaxies can be dominated by the thermal component. In such objects, both the radio and the infrared emission deviate significantly from the scaling relations with

star formation rate followed by more massive galaxies (Hunt et al. 2005, and references therein) : the radio continuum is depleted because of the delayed injection of cosmic rays in a young starburst, and possibly because of enhanced cosmic ray escape ; and the infrared emission is depleted because of lower dust content, different dust properties, and higher porosity of the interstellar medium.

We selected the galaxies that we term nascent starbursts from an infrared flux-limited sample by their high infrared to radio flux ratios and their high dust temperatures (Roussel et al. 2005). These criteria are designed to select galaxies hosting very young starbursts, like the galaxies mentioned above, but constituting a very different population: their infrared luminosities are much higher, they are more massive, and if cosmic ray escape is less efficient than in dwarfs, the radio deficiency also implies that cosmic rays produced by past star formation episodes have decayed, and thus have been injected more than ~ 100 Myr ago. In other words, the intensity contrast between the current starburst and the past star formation integrated over several tens of million years is very high. While classical starburst galaxies also contain very young star forming sites, our view of these is confused by recurrent burst episodes or continuous star formation in the recent past, which produce average signatures typical of evolved bursts, mimicking single populations of ages $\sim 5\text{--}10$ Myr (e.g. Calzetti 1997). Nascent starbursts, on the other hand, offer an ideally simplified view because of the dominance of a single and quasi-instantaneous burst of star formation (previous stellar generations being too old to contribute to the production of star formation tracers).

The nascent starbursts are extremely rare. They represent a negligible fraction ($\approx 1\%$) of an infrared flux-limited sample in the local universe such as the IRAS Faint Galaxy Sample, and about 16% of galactic systems whose flux density is higher at $60\,\mu\text{m}$ than at $100\,\mu\text{m}$ (Roussel et al. 2003). These objects nevertheless deserve careful study, because they constitute ideal settings to better understand the initial conditions and early evolution of starbursts, as well as the regulation of the infrared-radio correlation.

In such objects, where the active regions are very young and compact, the most useful diagnostics on the nature of the heating source are expected to arise from the dust and the molecular gas phases, because ultraviolet radiation will be confined to dense ultracompact HII regions (Habing & Israel 1979). The mid-infrared spectral range is of particular interest not only to constrain the nature and excitation of the small-size dust grains and aromatic compounds, but also because it contains a series of forbidden and molecular hydrogen lines providing unique diagnostics on HII regions, photodissociation regions, and the outer layers of molecular clouds, and which are much less affected by extinction than the other diagnostics accessible in the optical and near-infrared domains. An ISOPHOT mid-infrared spectrum of NGC 1377 between 2.5 and $4.8\,\mu\text{m}$ and between 6 and $11.5\,\mu\text{m}$ was presented by Laureijs et

al. (2000), as part of a small sample of galaxies whose infrared flux density distribution peaks at $60\,\mu\text{m}$. This spectrum appeared very peculiar in comparison with normal galaxies, containing a broad emission feature between 6 and $8.5\,\mu\text{m}$ in place of aromatic bands universally found in metal-rich star-forming galaxies, but lacked sufficient wavelength coverage to draw conclusions regarding the nature of the source and the excitation mechanisms of the dust and gas. NGC 1377 was selected to be part of the Spitzer Infrared Nearby Galaxies Survey (SINGS) sample (Kennicutt et al. 2003) to extend the range of explored $F_{60\,\mu\text{m}}/F_{100\,\mu\text{m}}$ ratios, indicative of average dust temperatures. In this paper, we present the SINGS broadband imaging data (3 to $160\,\mu\text{m}$) and spectral imaging data (with continuous coverage between 5 and $38\,\mu\text{m}$) of NGC 1377, as well as ancillary optical imaging and spectroscopic data obtained for SINGS. We analyze them in view of constraining the geometry of the gas and dust reservoir, the excitation of the different phases of the interstellar medium probed in the $5\text{--}38\,\mu\text{m}$ range, and what these properties imply for the nature of the activity in NGC 1377. The hypothesis of non-stellar activity is discussed in Section 9.

2. SINGS data

2.1. Spitzer spectral maps

Low spectral resolution cubes ($\lambda/\Delta\lambda \approx 60\text{--}130$) between 5 and $38\,\mu\text{m}$ and high spectral resolution cubes ($\lambda/\Delta\lambda \approx 600$) between 10 and $37\,\mu\text{m}$ centered on the nucleus of NGC 1377 were acquired with the IRS instrument (Houck et al. 2004a) in February 2005 and August 2004, respectively. For each spectral resolution mode, the full wavelength range is covered in two parts by two different slits: at low resolution, SL (5– $14.5\,\mu\text{m}$) and LL (14– $38\,\mu\text{m}$); and, at high resolution, SH (10– $19.5\,\mu\text{m}$) and LH (19– $37\,\mu\text{m}$). Quadruple coverage is obtained at each point of the maps, except at the edges, by moving the slit in increments of half the slit size in each direction (see Kennicutt et al. (2003) and Smith et al. (2004) for details on the observing strategy in SINGS). Given that the infrared emission of NGC 1377 is not spatially resolved (Section 3), all the emission is recovered within the spectral maps, the smallest of which, in the SH module, is $23''\times 15''$. The data were pre-processed with the S12 version of the Spitzer Science Center pipeline, and then assembled in spectral cubes with Cubism. Cubism is the software developed to rectify, project and co-add SINGS data, with the capability to subtract a spectral cube of the background and foreground (zodiacal) emission extracted from the data themselves, to mask pixels exhibiting an abnormal responsivity, and to perform spatial and spectral extractions (Smith et al., 2006, in preparation). In order to improve the signal to noise ratio of the high-resolution spectral data, an extra step was included in the processing of these data, outside of Cubism. In the SH and LH modules, the slit is

very narrow, only 6 pixels-wide on average, and the pixels with an abnormal responsivity are more numerous than in the SL and LL modules. Because of the minimal redundancy, masking pixels can create spurious features in the final cube. To mitigate this effect, the stacked diffraction images were inspected for obvious deviant pixels (i.e. features that are narrower than the spectral and spatial resolution), and these pixels were interpolated in each pointing along the wavelength dimension. This treatment is appropriate for infrared point sources like NGC 1377, with abrupt spatial variations and a smoothly-varying continuum, and leaves intact real spectral features.

2.2. Spitzer broadband imaging

Images in the four bands of the IRAC camera (Fazio et al. 2004), centered at effective wavelengths of 3.6, 4.5, 5.7 and 7.9 μm (usually designated by their fiducial wavelengths 3.6, 4.5, 5.8 and 8.0 μm), were obtained in August 2004. Scan maps in the three bands of the MIPS instrument (Rieke et al. 2004) at effective wavelengths of 24, 71 and 156 μm (fiducial wavelengths of 24, 70 and 160 μm) were acquired in September 2004. The observing strategy and data reduction are described by Kennicutt et al. (2003). The full width at half maximum of the point spread function (PSF) is close to 2.0'' at 7.9 μm , or 200 pc at the distance of NGC 1377 (21 Mpc). Flux calibration uncertainties are of the order of 10% in the IRAC bands, and 5%, 10% and 15% in the MIPS 24, 71 and 156 μm bands.

Broadband infrared flux densities of NGC 1377 are listed in Table 1. In the IRAC short-wavelength bands, both the total fluxes and the nuclear fluxes are provided. In all IRAC bands, the nuclear fluxes were measured within the smallest point-source aperture of diameter 4.88'', with a background annulus of internal and external diameters of 4.88'' and 14.64'', in which case aperture correction factors ranging from 1.213 to 1.584 are necessary (IRAC handbook). Use of the other point-source apertures tabulated in the IRAC handbook, for the 5.7 μm and 7.9 μm bands, leads to fluxes higher by up to 8% and 15% respectively. The smallest aperture is preferable in our case to minimize contamination by ghosts and other artifacts (see Section 3). It is also preferable, for the 3.6 μm and 4.5 μm bands, because the underlying disk emission is non-negligible at these wavelengths (see Table 1). No extended emission is detected in the 5.7 and 7.9 μm bands, and total fluxes measured in a large aperture (with correction factors of 0.63 and 0.69, respectively, that are appropriate for extended emission) are lower than the nuclear fluxes by 25% and 6% respectively. Since the aperture correction factors for extended emission are much more uncertain than for point sources, we adopt the nuclear fluxes as total measurements in the 5.7 and 7.9 μm bands. For the total fluxes in the 3.6 and 4.5 μm bands, we applied correction factors of 0.94 (IRAC handbook).

As the MIPS detectors do not suffer from the light scattering phenomenon making accurate photometry difficult in IRAC images, fluxes in the MIPS bands were simply measured by summation over the whole extent of the source.

2.3. Optical imaging and spectroscopy

Images in the B, V, R and I bandpasses were acquired at the CTIO 1.5 m telescope with the CFCCD (Cassegrain Focus CCD) instrument, in October 2001. The pixel size is $0.43''$ and the angular resolution (full width at half maximum), measured on stars nearby NGC 1377, varies between $1.15''$ and $1.23''$ in the different bandpasses. For comparison between the B band and the I band, the images were registered using the positions of a dozen stars, with a residual radial dispersion of $0.2''$, and convolved to a common resolution of $1.5''$.

Optical long-slit spectra between 3600 and 6900 Å, at a spectral resolution of 8\AA , were acquired at the Steward Observatory 2.3 m telescope in November 2001. The observations and data reduction are described by Moustakas et al. (2006, in preparation). We used an extraction aperture of $2.5'' \times 10''$ centered on the nucleus of the galaxy and oriented along the minor axis.

2.4. Flux calibration of the infrared spectra

The default flux calibration of Spitzer spectral data is appropriate only for staring observations of point sources, in which the loss of flux due to the diffraction beam being larger than the slit width is indirectly corrected for, by matching staring observations of stars with spectrophotometric models. Additional steps are necessary to calibrate mapping observations of arbitrarily-shaped sources. Although NGC 1377 is a point source in the infrared (Sect. 3), we cannot use the default flux calibration because it was not perfectly centered in the slits. The flux loss fraction as a function of wavelength was derived from estimates of the beam profile using the PSF simulator distributed by the Spitzer Science Center.¹ The spectra of the galaxy were then corrected by this function to remove the added point-source flux falling outside the central slit, because this flux is already retrieved by mapping the source. For the low-resolution data, it is also necessary to correct for the fact that the default flux calibration is done by extracting stellar spectra within an aperture much smaller than the

¹<http://ssc.spitzer.caltech.edu/archanaly/contributed/browse.html>

slit length. The conversion from e^-/s units to flux density units using the full slit length was derived from highly redundant observations of the calibrating stars HR 6688 (for the LL module) and HR 7891 (for the SL module), mapped in the slit-parallel direction. The spectra of these stars, extracted in an aperture of the same width as that used for NGC 1377, were divided by model spectra from Decin (2004)² to derive the flux calibration functions. These functions were adjusted with smoothly-varying polynomials before being used to divide the LL and SL spectra of NGC 1377. Broadband photometry in the IRAC, MIPS and ISOCAM filters was then simulated from the spectra, using the appropriate transmission curves, and compared with imaging photometry. We obtain excellent agreement at $24\mu m$ and $5.7\mu m$: $F_{24}(\text{MIPS})/F_{24}(\text{LL}) = 1.01$ and $F_{5.7}(\text{IRAC})/F_{5.7}(\text{SL}) = 0.98$. The agreement with ISOCAM data is also quite good despite uncertainties in the saturation correction in the images (for details, see Roussel et al. 2003): $F_{6.7}(\text{ISOCAM})/F_{6.7}(\text{SL}) = 0.88$ and $F_{15}(\text{ISOCAM})/F_{15}(\text{SL} - \text{LL}) = 0.97$. Note that the spectral shape between 13 and $14.5\mu m$ is not well calibrated at low resolution, because of an artifact at the 10% level in the detector, which cannot be modelled at present. Comparison with SH data, which are not affected by this artifact, however shows good consistency. We also obtain $F_{7.9}(\text{IRAC})/F_{7.9}(\text{SL}) = 0.92$. Since IRAC photometry is itself uncertain (see Sect. 2.2), this does not imply any significant error in the spectral flux calibration.

3. Morphology and general properties

NGC 1377 is a member of the unrelaxed Eridanus galaxy group (Willmer et al. 1989), at an estimated distance of 21 Mpc . In stellar light, it has the appearance of a regular lenticular galaxy, with a diameter of $1.8'$ (about 11 kpc) at the 25 mag/arcsec^2 blue isophote, an axis ratio close to 2.0 , and a position angle of 92° (de Vaucouleurs et al. 1991). Heisler & Vader (1994), based on optical imaging of NGC 1377 as part of a sample of galaxies with $F_{60\mu m} > F_{100\mu m}$, mentioned the presence of a dust lane along the southern part of the minor axis, in an otherwise featureless morphology. The far-infrared (40 – $120\mu m$) luminosity of NGC 1377, as derived from the IRAS 60 and $100\mu m$ fluxes, is $4.3 \times 10^9 L_\odot$. The center of the galaxy contains a compact molecular gas reservoir of $2 \times 10^8 M_\odot$ or more, about ten times more massive than the amount of gas expected to be associated with the dust seen in emission (see Section 6), if a Galactic gas to dust mass ratio is assumed (Roussel et al. 2003). The molecular gas properties are similar to those characterizing starbursts: the far-infrared to CO flux ratio is seven times higher than in normal galaxies and the gas is subthermal.

²The data are made available at the web address: <http://ssc.spitzer.caltech.edu/irs/calib/templ/>.

Figure 1 shows the (B-I) color map derived from the optical images obtained for SINGS. The disturbance noted by Heisler & Vader (1994) is readily apparent, but seems more complex than a single dust lane. Two main orthogonal red features are surrounded by more diffuse red filaments. The color excess between the central feature and the normal light distribution immediately to the north is approximately 0.9 mag. The residuals from the B-band image after subtraction of a smooth symmetric photometric model are shown in Figure 2. Some faint arcs of excess light are seen in the center, as well as to the north-east and to the south-east of the central regions. Negative residuals of large amplitude, that may be interpreted as regions of excess obscuration and thus excess column density of cold dust and gas, are seen in the nucleus and several pockets immediately to the south. In addition, a straight lane extends further to the south, and diffuse structures further to the west. These faint residuals are discernible out to about 2 kpc in projected distance from the nucleus. The overall morphology suggests a recent merging event with one or several small bodies, in which the structure of NGC 1377 would have been preserved. As NGC 1377 is very deficient in atomic hydrogen gas, more robust evidence cannot be obtained from HI observations but would require high spectral resolution and high sensitivity observations of the stellar and molecular gas kinematics.

The infrared images from 3.6 to 24 μm are shown in Figure 3. They are dominated by a very bright nucleus. At 3.6 and 4.5 μm , the underlying smooth emission from the old stellar disk is also visible, with the same distribution as the I-band light. The reticle-shaped artifact in the 4.5 μm image (with orthogonal positive and negative rows) is produced by the “multiplexer bleed” and “pull-down” effects, respectively, typically associated with bright point sources (IRAC handbook). At 5.7 μm , the stellar disk emission has fallen below the sensitivity limit, and only the nucleus is detected at longer wavelengths. It has the appearance of the point response functions of the IRAC and MIPS detectors, with bright diffraction spikes. The rows that are bright throughout the field of view of the 5.7 and 7.9 μm images exemplify the “pull-up” and “optical banding” artifacts (IRAC handbook). Since existing corrections of these artifacts are only cosmetic, we did not apply them but masked out the affected rows and columns in our analysis.

To decompose the nuclear 7.9 μm source and determine whether its size is measurable, point spread functions (PSF) derived from observations of bright stars are not appropriate, because their cores are more extended than the observed core of NGC 1377, sampled at the native IRAC pixel size of 1.22''. This is probably because the spectral slope of NGC 1377 within the 7.9 μm filter bandpass is much steeper than that of stars (the flux density decreasing sharply from 7.8 μm to 9.5 μm , because of the deep flanking silicate absorption), and the PSF width depends on the spectral slope, increasing as the spectrum reddens. The model PSFs computed with the tool provided by the Spitzer Science Center, “S-Tiny Tim”, using

the spectrum of NGC 1377, are also inappropriate for our purpose, because they depend on pre-launch characteristics and are not accurate enough. Within the uncertainties on the PSF, the mid-infrared source in NGC 1377 is thus not resolved. Both this constraint and that obtained previously on the size of the $2.12\text{ }\mu\text{m}$ molecular hydrogen line emission (Roussel et al. 2003) imply that the region of activity is less extended than $\sim 1''$, i.e. $\sim 100\text{ pc}$. To look for asymmetries in the $7.9\text{ }\mu\text{m}$ emission, we extracted one half of the map on the left side of the vertical symmetry axis of the diffraction and “pull-up” pattern (the tilted upper half in Figure 3), and subtracted the mirror image from the other half of the map. The result is shown in Figure 4. The residuals do not include any extended emission, but primary and secondary ghosts of the nucleus, as well as the real source labelled A. Given its detection in the optical bands and its approximate fluxes in the IRAC bands, this source contains both stellar and dust components, and is likely a distant galaxy.

4. Optical spectroscopy

Optical slit spectroscopy shows the [NII] line at 6583 \AA and the [SII] lines at 6716 and 6731 \AA in emission without any detection of $\text{H}\alpha$ (Kim et al. 1995). Our long-slit data confirm this result (Fig. 5). The [OIII], [OII] and $\text{H}\beta$ emission lines are not detected either. As the optical depth of the infrared source is extremely high (Sect. 6), we infer that [NII] and [SII] arise in the foreground. Even accounting for underlying stellar absorption in the $\text{H}\alpha$ line, the $[\text{NII}](6583\text{ \AA})/\text{H}\alpha$ ratio is constrained to be larger than unity. Since the lines cannot be excited by an active nucleus, because they do not probe the nuclear regions, they indicate shock excitation (Baldwin et al. 1981). In addition, the low $[\text{SII}](6731\text{ \AA})/[\text{SII}](6717\text{ \AA})$ ratio implies that they arise in regions of low electronic density (Dopita 1977).

Nebular diagnostics of metallicity are not useable in NGC 1377. Stellar absorption indices of metallic lines and $\text{H}\beta$, on the other hand, are measureable in the spectrum of NGC 1377. But they are degenerate with respect to age and metallicity, except for galaxies which have been passive for several gigayears, which appears not to be the case for NGC 1377: $\text{EW}(\text{Mg}_b) = 2.4\text{ \AA}$, $\text{EW}(\text{Fe}_{5270}) = 2.1\text{ \AA}$ and $\text{EW}(\text{H}\beta) = 3.3\text{ \AA}$ in the index definition of Worthey et al. (1994). However, the large quantity of CO gas and dust (Sect. 6), relative to the stellar emission, argues against NGC 1377 being a low-metallicity system.

The optical spectrum, covering a large wavelength interval (between 3600 and 6900 \AA), enables us to constrain the star formation history of NGC 1377. We used the population synthesis models of Bruzual & Charlot (2003) to fit the entire spectrum by a discrete sum of instantaneously-formed populations, as described by Moustakas & Kennicutt (2006), assuming solar metallicity and a Salpeter (1955) initial mass function. The estimated stellar

extinction is $A_V \sim 0.9$ mag in the screen hypothesis. We find that the light is dominated by populations older than 1 Gyr (~ 60 to 80% in the V band), and that the most recent star formation episode traceable in the optical occurred more than 500 Myr ago. This is fully consistent with the radio continuum upper limit indicating that the cosmic ray population generated by the last major star formation episode has decayed, implying that this episode occurred more than 100 Myr ago.

5. Infrared spectral energy distribution and spectral features

The entire infrared spectral energy distribution, including the low-resolution spectra, calibrated to reproduce the broadband photometry as explained in Section 2.4, is shown in Figure 6. To the far-infrared broadband fluxes, color corrections between 1.00 and 1.08 were applied. It is immediately apparent that the infrared source is not only very hot and thus compact (in agreement with the fact that it is not spatially resolved), but is also strongly self-absorbed, as shown by the deep absorption bands from amorphous silicates at 10 and 18 μm . The forbidden lines from HII regions and photodissociation regions that are bright in star-forming galaxies ([SiII], [SIII], [NeII], [NeIII]) are absent in NGC 1377 (Table 2), except for a very weak [NeII] line at 12.8 μm , which will be discussed in Section 7. The energy peak lies between 30 and 50 μm (Fig. 6b), which is extremely unusual, even for starburst galaxies. An even more extreme spectrum (with an energy peak around 15-20 μm) has been observed in SBS 0335-052, a blue compact dwarf galaxy of very low metallicity (Houck et al. 2004b). Since SBS 0335-052 contains one of the most deeply embedded super star clusters known, it may be instructive to compare it with NGC 1377. Their spectra suggest that the geometry of the source may be similar in both systems, compact and sharply bounded. There are however important differences. The mid-infrared emission of SBS 0335-052 between 5 and 10 μm is very faint, indicating that dust species related to the aromatic band carriers are absent and that very small grains are depleted with respect to big grains (Plante & Sauvage 2002). On the contrary, the mid-infrared emission of NGC 1377 accounts for a large fraction of the total infrared power and implies that very small grains are abundant (even though aromatic band carriers are seemingly absent), or alternatively that the radiation field intensity is high enough to heat big grains to very high temperatures. The optical depth in the amorphous silicate absorption bands is also much higher in NGC 1377.

No other spectral features are seen, except some molecular hydrogen rotational lines (Fig. 7), which will be discussed in Section 8, as well as a few broad emission features of very low intensity and weak absorption features from gas-phase molecules. Superposed on the deep 10 μm silicate absorption band, a very weak 11.3 μm emission band is detected, and

likely arises from polycyclic aromatic hydrocarbons (Fig. 8). This feature is well matched by the profile of the $11.3\,\mu\text{m}$ PAH band of the Orion bar (Peeters et al. 2004), at the spectral resolution of our data. It may originate from intermediate dust shells, with optical depths lower than the silicate optical depth, but still higher than unity (see below). The $11.3\,\mu\text{m}$ aromatic band is always observed in association with other bands, the most prominent of which lies at $7.7\,\mu\text{m}$. The non-detection of the $7.7\,\mu\text{m}$ band could easily be due to its being hidden in the observed broad $5\text{--}9\,\mu\text{m}$ bump, which peaks almost exactly at the central wavelength of the aromatic band (see Section 6). Likewise, a $12.7\,\mu\text{m}$ aromatic band, if present, could be hidden in the broad bump on the red shoulder of the $10\,\mu\text{m}$ silicate band (Fig. 6).

Another broad and faint feature is seen below the $17.03\,\mu\text{m}$ H_2 line, at the bottom of the $18\,\mu\text{m}$ silicate absorption band (Figure 8). It could be composed of the same bands at 17.1 , 17.4 and $17.8\,\mu\text{m}$ that were shown recently to be common in the interstellar medium of normal galaxies (Werner et al. 2004; Smith et al. 2004, 2006), and that are thought to be related to polycyclic aromatic hydrocarbons. Van Kerckhoven et al. (2000) have extracted a plateau of blended broad features attributed to the C-C-C bending modes of PAHs in this wavelength range (more exactly between 15 and $20\,\mu\text{m}$), in compact HII regions as well as young and evolved stars. They also state that small-size PAHs would have sharper spectral structure (in particular a band at $16.4\,\mu\text{m}$, unseen in NGC 1377) than bigger aromatic compounds. If the $16.5\text{--}18.5\,\mu\text{m}$ bump observed at the bottom of the $18\,\mu\text{m}$ silicate band in NGC 1377 is attributable to PAHs, then the lack of substructure would indicate a predominance of bigger aromatic compounds.

Finally, we tentatively detect two additional broad features at 6.3 and $6.7\,\mu\text{m}$ (Fig. 8). The dip longward of $6.8\,\mu\text{m}$ could be caused by an absorption from C-H bending modes of hydrocarbons at $6.85\,\mu\text{m}$, seen in deeply obscured infrared-luminous galaxies by Spoon et al. (2001) and Spoon et al. (2004). For comparison, Fig. 8 shows the spectrum of one of these galaxies, IRAS 08572+3915 (Spoon et al. 2006a), where the absorption bands from hydrocarbons at $6.85\,\mu\text{m}$ and $7.25\,\mu\text{m}$ are clearly seen. However, there is no known species being able to cause the dip at $6.5\,\mu\text{m}$. The $6.3\,\mu\text{m}$ band has been observed in at least two post-AGB stars by Peeters et al. (2002) and has also been invoked by Sturm et al. (2000) to explain the excess emission redward of the $6.2\,\mu\text{m}$ aromatic band of starburst galaxies. It has so far not been observed alone (without the $6.2\,\mu\text{m}$ band) in galaxies. According to Peeters et al. (2002), the class of PAHs with a $6.3\,\mu\text{m}$ peak wavelength may have a more pristine composition than the $6.2\,\mu\text{m}$ PAHs, and may not yet have been exposed to hard radiation. It can be expected from the compact starburst nature of NGC 1377 that PAHs have all been destroyed in the zone of activity and survive only in outer shells where they would not yet have felt the influence of the starburst ; it would however be difficult to understand how

they could have avoided some kind of processing. The as yet unidentified $6.7\,\mu\text{m}$ band has been observed in NGC 7023 (Werner et al. 2004) and in spiral galaxies (Smith et al. 2006).

If we assume that the intrinsic relative intensities of the 6.3 , 6.7 , $17\text{--}18$ and $11.3\,\mu\text{m}$ bands are similar to what is seen in normal galaxies, then they are not consistent with zero extinction, but would be consistent with an optical depth of the order of half the optical depth affecting the continuum (which is about 8.5 at $11.3\,\mu\text{m}$, as constrained in Sect. 6). Given the utter uncertainty on the relative geometry of the different dust phases, and the fact that the relative intensities of the aromatic bands are intrinsically variable in various interstellar sources and in galaxies (Peeters et al. 2002; Smith et al. 2006), the identification of the reported features with PAHs is therefore plausible.

Very faint absorption features are seen at high resolution between the two amorphous silicate bands: HCN at $14.03\,\mu\text{m}$, which lies at the end of two spectral orders but is confirmed in both, possibly C_2H_2 at $13.7\,\mu\text{m}$, and CO_2 at $15.0\,\mu\text{m}$, which lies at the end of a single spectral order and is outside the wavelength range of the adjacent order (Fig. 9). These absorption bands, tracers of hot dense gas, have been observed in deeply obscured infrared-luminous galaxies (Spoon et al. 2006b). Contrary to what is seen in some of the latter objects and in Galactic center sources (Chiar et al. 2000), we do not detect any absorption features in the $5\text{--}8\,\mu\text{m}$ range, i.e. from water ice at $6\,\mu\text{m}$ and from hydrocarbons at 6.85 and $7.25\,\mu\text{m}$.

6. Geometry and density

To attempt to constrain the geometry of the infrared source in NGC 1377, following the same approach as Plante & Sauvage (2002) for SBS 0335-052, we used the DUSTY radiative transfer model (Nenkova et al. 2000), assuming a unique, spherically-symmetric source. By construction, aromatic compounds are not included in the model, and impulsive heating³ of very small grains is not taken into account. This shortcoming is partially mitigated by the fact that the dust in NGC 1377 is heated to very high temperatures, and thus closer to thermal equilibrium than in normal starbursts, but the results should be interpreted with caution. However, we note that the effect of neglecting impulsive heating should produce residuals smoothly distributed in wavelength, not narrow features (see below). Another important limitation is that the same grain size distribution has to be postulated for all dust species, despite the fact that all the families of dust models of the local interstellar medium need very different size distributions for silicates and carbon-based dust (Zubko et al. 2004). Since no unique set of geometric parameters will provide a fit to the data, and

³also referred to as transient, stochastic, or single-photon heating

extensive exploration of the parameter space would be prohibitively long for such a high optical depth as seen in NGC 1377, we restrict the analysis to a qualitative assessment of the density. For the silicate grains, we find that, among the choices available within DUSTY, the optical properties of Ossenkopff et al. (1992) allow the best reproduction of the shape of the silicate absorption bands. For the carbonaceous grains, graphite, with the optical properties of Draine & Lee (1984), allows a better fit to the spectrum of NGC 1377 than amorphous carbon.

Figure 10 shows fits reproducing the available data from 3.6 to $156\mu\text{m}$, except in a few wavelength intervals that will be discussed separately below. The models contain at least 70% of amorphous silicates by number of grains, which corresponds to about 80% of silicates by mass, using the mass densities provided by Weingartner & Draine (2001) and Laor & Draine (1993). This mass abundance is a bit larger than required by the relevant class of dust models of Zubko et al. (2004) ($\sim 66\%$), as well as by the dust model of Li & Draine (2001) ($\sim 73\%$). Such a large fraction of silicates is made necessary in NGC 1377 to account for the great depth of the $10\mu\text{m}$ and $18\mu\text{m}$ features. It can be speculated that this reflects composition changes effected by the intense radiation in the starburst region, silicates possibly being more resilient than carbonaceous grains in an oxygen-rich medium. The best fits are also obtained for a grain size distribution enhanced in small grains, with a power-law index -5 instead of -3.5 (for the standard Mathis et al. (1977) distribution) and a lower cutoff of the order of 10\AA . In particular, for a normal size distribution, the opacity would have to be much higher in order to reproduce correctly the $10\mu\text{m}$ and $18\mu\text{m}$ absorption bands. This may be an artifact of the model, compensating for the absence of impulsive heating.

The model implies an opacity of at least 75 in the V band, more than 20 at the center of the $10\mu\text{m}$ silicate band, and about 10 in the $18\mu\text{m}$ silicate band. The radial density profile, that was parameterized as a broken power-law, is very steep, with an index of -2 in the center and -1.5 outside. The density profile in the outer parts is ill-constrained, and does not allow us to derive a total size. For a bolometric luminosity of $1.1 \times 10^{10} L_\odot$, derived from the data themselves by integration over the whole infrared spectral energy distribution, and a temperature of 2000 K at the inner surface of the dust shell, the radius of this inner layer is constrained to be 0.08 pc, very similar to what Plante & Sauvage (2002) found for SBS 0335-052, although the total infrared luminosity of NGC 1377 is about three times higher (the inner dust temperature of the model of SBS 0335-052 is only 700 K). The dust mass derived from the $60\mu\text{m}$ and $100\mu\text{m}$ fluxes, using the Galactic emissivity as formulated by Bianchi et al. (1999), is $2.7 \times 10^5 M_\odot$. It can alternatively be derived from the opacity obtained with

the DUSTY model:

$$\tau_V = \sum_i (f_i \kappa_{Vi} \rho_i) \int_a (4/3\pi a^3 n(a) da) \int_r (N(r) dr)$$

and $M_{\text{dust}} = \sum_i (f_i \rho_i) \int_a (4/3\pi a^3 n(a) da) \int_r (N(r) 4\pi r^2 dr),$

where the index i designates each dust species (here silicates and graphite), f_i is their fraction by number, κ_{Vi} is their mass absorption coefficient in the V band, ρ_i is the solid density of the grains, $n(a) da$ the grain size distribution and $N(r) dr$ the radial density distribution adopted in the model. It follows that

$$M_{\text{dust}} = 4\pi \tau_V \frac{\sum_i (f_i \rho_i)}{\sum_i (f_i \kappa_{Vi} \rho_i)} \frac{\int_r (N(r) r^2 dr)}{\int_r (N(r) dr)}.$$

We used $\kappa_V = 0.3 \text{ m}^2 \text{ g}^{-1}$ for silicates and $5 \text{ m}^2 \text{ g}^{-1}$ for graphite (Draine & Lee 1984) ; and $\rho = 3.5 \text{ g cm}^{-3}$ for silicates and 2.24 g cm^{-3} for graphite (Weingartner & Draine 2001; Laor & Draine 1993). Varying the V-band optical depth between 75 and 95 (Fig. 10), we obtain a dust mass in the range $(2.6\text{--}3.3) \times 10^5 \text{ M}_\odot$, in good agreement with the determination from the far-infrared fluxes. Assuming a gas to dust mass ratio of 100 (Sodroski et al. 1994), we obtain a central gas density of about $3 \times 10^4 \text{ M}_\odot \text{ pc}^{-3}$, or equivalently a hydrogen nucleus density of 10^4 cm^{-3} .

It should be noted here that the observations up to $156 \mu\text{m}$ are not sensitive to the potential presence of very cold dust (not illuminated by the starburst). Our dust mass estimates are therefore lower limits, and we suspect the total dust mass to be about ten times higher, since the mass of cold molecular hydrogen is ten times higher than the mass of gas expected to be associated with the dust seen in emission.

The residuals, after subtraction of the model (Fig. 11), can tentatively be identified with emission bands from aromatic compounds and absorption bands from crystalline silicates. If the identification with aromatic band carriers is correct, their chemical composition is likely different from those dominating the mid-infrared spectrum of normal star-forming galaxies, as indicated by the absence of the $6.2 \mu\text{m}$ band near the $6.3 \mu\text{m}$ band (Section 5). In Figure 11a, prominent features are seen at peak rest wavelengths of 7.7 and $12.7 \mu\text{m}$. Note that the absorption profile of silicates is not perfectly reproduced ; it might be possible to explain the excess emission by a combination of impulsive heating (neglected in the model) and modified optical properties of silicates.

Absorption bands from crystalline silicates have been found in some infrared-luminous galaxies by Spoon et al. (2006a). In Figure 11b, features are seen at rest wavelengths of

23.5 and 28 μm . Other known features from forsterite exist at 16 and 19.5 μm , but the quantification of their depth in NGC 1377 is made hazardous by the possible contamination by aromatic bands in the 17–18 μm range (Fig. 8). The 16 μm band, in particular, would have to be shifted to longer wavelengths in comparison with IRAS 08572+3915. Another feature exists at $\approx 11 \mu\text{m}$, but there again it is confused by the 11.3 μm PAH. Crystalline forsterite also produces strong bands at about 34 and 70 μm , among others (Koike et al. 1993; Molster et al. 2002). The dip of the spectrum of NGC 1377 at the long-wavelength end of the LL1 module, between 30 and 35 μm (Fig. 6 and 11) may be attributed to absorption by crystalline silicates. Likewise, they may contribute, at least partially, to the weakness of the 71 μm broadband flux relative to the 60, 100 and 156 μm fluxes.

7. Forbidden lines

Mid-infrared forbidden lines are important tracers of HII and photodissociation regions, and of the physical conditions therein. Figure 9 shows the detection of a very weak [NeII] line. [NeII] emission without detection of any other forbidden line in the mid-infrared range is also observed in some galaxies of the sample of Spoon et al. (2006a). We attempt here to extract, from the detection of [NeII] and the absence of other lines, constraints on the recombination rate and electronic density. The low signal to noise ratio of [NeII] precludes measuring the line width accurately, but it is well matched by the spectral resolution (corresponding to a full width at half maximum of 500 km s^{-1} for an unresolved line).

The estimated flux (Table 2) can be translated into a recombination rate. We have

$$F_{[\text{NeII}]} \times 4\pi D^2 = h\nu V C N(\text{Ne}^+) N(\text{e}^-) (T_e/1 \text{ K})^{-0.5} \Omega(T_e) g_l^{-1} \exp(-h\nu / (kT_e))$$

and $N_r = \alpha(T_e) V N(\text{H}^+) N(\text{e}^-)$, where D is the distance of NGC 1377, V is the volume of the HII region, $C = 8.6287 \times 10^{-6} \text{ cm}^3 \text{ s}^{-1}$, N designates a volume density, $\Omega(T_e)$ is the collision strength, g_l is the statistical weight of the ground level (4 for [NeII] and 5 for [NeIII]), and $\alpha(T_e)$, which depends only weakly on the electronic density, is the hydrogen recombination coefficient. We assume that $N(\text{Ne})/N(\text{H}) = [N(\text{Ne}^+) + N(\text{Ne}^{2+})]/N(\text{H}^+)$ and that the neon abundance is equal to the solar value, 6.9×10^{-5} (Asplund et al. 2004). The collision strengths of the [NeII] and [NeIII] transitions are tabulated respectively by Saraph & Tully (1994) and Butler & Zeippen (1994), and the hydrogen recombination coefficient by Storey & Hummer (1995). Accounting for the upper limit on the [NeIII] line flux and assuming that the electronic temperature is between $5 \times 10^3 \text{ K}$ and 10^4 K , we obtain a recombination rate (uncorrected for the extinction in the [NeII] and [NeIII] lines) $N_r = (5.7 \pm 1.6) \times 10^{51} \text{ s}^{-1}$.

The upper limit on the thermal emission at 3 cm (Roussel et al. 2003) independently

provides an upper limit on the recombination rate: $N_r < (T_e/10^4 \text{ K})^{-0.45} \times 5.4 \times 10^{52} \text{ s}^{-1}$, which is at least an order of magnitude smaller than the intrinsic ionizing photon flux N_{Lyc} , because most of the ionizing photons are absorbed by dust. The estimate derived from the [NeII] line is consistent with this limit provided that the optical depth in the line be lower than 2.6. The modelled optical depth at the wavelengths of both [NeII] and [NeIII] is however of the order of 6.5 (Sect. 6). This discrepancy calls for at least one remark: if the starburst is not made of a unique stellar cluster but occurs simultaneously at several locations (Sect. 6), then the [NeII] line emission may arise from the regions of lowest optical depth.

The upper limits obtained on the hydrogen recombination lines (Roussel et al. 2003) provide another constraint on the nebular extinction. The requirement that the recombination rates derived from the 3 cm, [NeII], Br γ and Pa β measurements be all consistent implies a nebular optical depth of $0.9 < \tau(12.8 \mu\text{m}) < 2.6$, assuming the Galactic center extinction law of Moneti et al. (2001).

We have assumed that collisional de-excitation is negligible. If this were not the case, then our estimate of the apparent ionizing photon flux would be underestimated, and the optical depth in the [NeII] line would have to be even lower. The data do not provide any constraint on the electronic density, but the radiative transfer model (Sect. 6) suggests a central gas density of the order of 10^4 cm^{-3} . To determine whether the mid-infrared nebular lines can be suppressed by collisional de-excitation in NGC 1377, we computed the critical densities of the ionic lines that are usually the brightest between 10 and $35 \mu\text{m}$ in star-forming galaxies, and that are tabulated in Table 2. If the electronic density is below the critical densities, then we expect minimum line ratios $F_{[\text{SIII}]}/F_{[\text{NeII}]} \sim 0.5$, $F_{[\text{SIII}]\,33.5 \mu\text{m}}/F_{[\text{NeII}]} \sim 0.15$ and $F_{[\text{SIII}]\,18.7 \mu\text{m}}/F_{[\text{NeII}]} \sim 0.2$. These values are derived empirically from the lower bounds observed in nuclei within the rest of the SINGS galaxy sample ; they correspond to the theoretical values if $\approx 60\%$ of gas-phase silicon is in Si $^+$ assuming that $\approx 90\%$ of silicon atoms are retained in dust grains, and $\approx 5\%$ of sulfur is in S $^{2+}$, with the Si and S solar abundances given by Grevesse & Sauval (1998). The upper limits obtained for NGC 1377 are above these minimum ratios, except $F_{[\text{SIII}]\,18.7 \mu\text{m}}/F_{[\text{NeII}]} < 0.12$. Since an optical depth of ~ 1 in [NeII] (corresponding to an optical depth of the same order in [NeIII]) is sufficient to explain this low ratio, we are unable to set constraints on the electronic density. Collisional de-excitation may not operate for [NeII] and [NeIII], since their critical densities are at least ten times higher than the neutral density estimate from the radiative transfer model. It should be noted, on one hand, that the peak density could be significantly higher than our estimate, and, on the other hand, that the electronic density should be much lower than the neutral density if pressure equilibrium is maintained. It is thus unlikely that [NeII] and [NeIII] be collisionally de-excited.

8. Molecular hydrogen

NGC 1377 is the only member of the SINGS sample in which H_2 lines dominate the line spectrum in the mid-infrared (and also in the near-infrared). Three rotational transitions of H_2 have been confidently detected: the S(1) and S(2) transitions at high spectral resolution, and the S(3) transition at low resolution in the SL1 module (Fig. 7). The line fluxes are given in Table 2. Based on previous observations of rovibrational transitions in the near-infrared, we had concluded that H_2 is collisionally excited (pure fluorescence being ruled out by the high flux ratio of the $v=1-0$ S(1) transition to the $v=2-1$ S(1) transition), and that slow shocks in the molecular phase are responsible (Roussel et al. 2003). The alternative mechanism, collisions with hot hydrogen atoms and molecules in dense photodissociation regions (Hollenbach & Tielens 1997, and references therein), seems indeed in conflict with the expectation that photoelectric heating will be inefficient in NGC 1377, because small dust grains may be positively charged due to the very intense radiation field. This effect was observed by Malhotra et al. (2001) for the [CII] and [OI] lines at $157.7\text{ }\mu\text{m}$ and $63.2\text{ }\mu\text{m}$, which are among the most efficient coolants of photodissociation regions. They were not detected by ISO-LWS observations in NGC 1377 (Roussel et al. 2003). The power emitted in the sum of the S(1) to S(3) transitions of H_2 represents a fraction $\sim 6 \times 10^{-4}$ of the far-infrared luminosity ($40\text{--}120\text{ }\mu\text{m}$) ; and the upper limits on the [CII] and [OI] luminosities respectively $\sim 6 \times 10^{-4}$ and $\sim 9 \times 10^{-4}$.

Using the recent photodissociation region models of Kaufman et al. (2006), we can test whether this excitation mechanism is efficient enough to account for the observed brightness of the H_2 lines. In these models, the maximum fraction of the far-ultraviolet radiation (FUV, between 6 and 13.6 eV) emerging in the rotational S(1) line is $\sim 10^{-3}$, and it occurs for a radiation field intensity of $G_0 \sim 200$ times the local value and densities of $n \sim 10^4\text{ cm}^{-3}$. At higher G_0 values, the gas heating efficiency declines ; and at higher densities, the gas cools partially through collisions with dust grains (Hollenbach & Tielens 1997). The H_2 line flux ratios of NGC 1377 ($F_{\text{S}(1)}/F_{\text{S}(0)} > 7$, $F_{\text{S}(2)}/F_{\text{S}(0)} > 4$, $F_{\text{S}(3)}/F_{\text{S}(1)} \geq 1$ and $F_{v=1-0\text{S}(1)}/F_{v=2-1\text{S}(1)} > 30$, these limits accounting for any amount of extinction) indicate that $G_0 > 10^4$ and $10^5 < (n/\text{cm}^{-3}) < 10^7$; and under these conditions, the maximum $F_{\text{S}(1)}/\text{FUV}$ flux ratio is $\sim 4 \times 10^{-4}$. In NGC 1377, the 3 cm upper limit implies that the part of the ionizing photon flux N_{LyC} escaping dust absorption is $< 7.4 \times 10^{52}\text{ s}^{-1}$, and $L_{\text{FUV}} \sim 5.1 \times 10^{-18}\text{ W} \times (N_{\text{LyC}}/\text{s}^{-1})$ for a 1 Myr-old starburst with a Salpeter initial mass function (using the population synthesis model of Leitherer et al. (1999)). Therefore, we expect to observe a maximum of $\sim 30 \times 10^{-18}\text{ W m}^{-2}$ in the $v=0$ S(1) line.

The observed flux is twice as high. The intrinsic flux can be much higher, if it is affected by the same optical depth as toward [NeII], since gas heated in photodissociation regions

would have to be located very close to the HII regions. The minimum optical depth toward [NeII] (Section 7) would correspond to $\tau(17\mu\text{m}) \sim 1.1$. The intrinsic flux in the H_2 $v=0$ S(1) line would therefore be about six times higher than the model prediction. This difference is marginal, compared with model uncertainties, in particular on the H_2 collisional de-excitation rates. However, we note that the $\text{Br}\gamma$ to H_2 $v=1-0$ S(1) flux ratio (which is immune to extinction effects if the emission is nearly cospatial) is lower than 0.1 in NGC 1377 (Roussel et al. 2003), which is much lower than expected in the case of photodissociation region heating of H_2 . For example, the normal starburst NGC 1022 has a $\text{Br}\gamma$ to H_2 $v=1-0$ S(1) flux ratio of 2.2. We thus argue that shock excitation plays a dominant role in NGC 1377, although photodissociation region models are marginally consistent with the present data.

An excitation diagram combining all the observed transitions to date (Fig. 12) confirms collisional excitation, and allows us to set a constraint on the amount of extinction in the H_2 lines, as explained below. The flux of a transition $v \rightarrow v' J \rightarrow J - 2$ is given by $F = h\nu A N_{\text{u, col}} \Omega / (4\pi)$, where $N_{\text{u, col}}$ is the column density of molecules in the upper level, A is the spontaneous emission probability, $h\nu$ is the transition energy and Ω is the source solid angle. We also have $N_{\text{u}} = g_{\text{u}} N_{\text{tot}} \exp(-E_{\text{u}} / (kT)) / Z(T)$, where $g_{\text{u}} = (2i + 1) (2J + 1)$ is the statistical weight (with the spin number $i = 0$ for even J or para transitions, and $i = 1$ for odd J or ortho transitions), $Z(T) \sim 0.0247 T / (1 - \exp(-6000 \text{ K} / T))$ is the partition function, and E_{u} is the upper level energy (Herbst et al. 1996). Line ratios thus allow the derivation of an apparent excitation temperature:

$$kT = (E_{\text{u2}} - E_{\text{u1}}) / \ln(N_{\text{u1}}/N_{\text{u2}} \times g_{\text{u2}}/g_{\text{u1}})$$

with $N_{\text{u1}}/N_{\text{u2}} = F_1/F_2 \times A_2/A_1 \times \lambda_1/\lambda_2$.

We used the spontaneous emission probabilities given by Turner et al. (1977). Since the temperature constrained by the rotation-vibration S(0) lines and by the rotation-vibration S(1) lines is consistent with the temperature derived from the pure-rotation transitions, collisional excitation is confirmed.

In order for the excitation temperature to remain monotonic as a function of the upper level energy (T increasing as E_{u} increases), the equivalent V-band optical depth has to be lower than 17 ($\tau < 1.1$ at $17\mu\text{m}$). This estimate takes into account the errors on the line fluxes, and assumes that H_2 at all temperatures is affected by a same extinction following the Galactic center extinction law of Moneti et al. (2001). Since the optical depth in the dust phase is much higher, most of the detected molecular hydrogen must come from intermediate layers. For zero extinction, the excitation temperature varies from (365 ± 50) K for the low-energy transitions, to (610 ± 25) K between the $v=0$ S(3) and $v=1-0$ S(1) transitions, to < 1500 K for the higher-energy transitions ; for the maximum allowed extinction, it varies between 420 K and < 1350 K.

Computing the mass of warm molecular hydrogen from the flux of the S(1) transition and the temperature derived from the rotational lines, we obtain $7.2 \times 10^5 M_\odot$ in the hypothesis of zero extinction, and $1.9 \times 10^6 M_\odot$ with $\tau_V = 17$. Since we had derived a total molecular hydrogen mass of the order of $2 \times 10^8 M_\odot$ from CO observations (Roussel et al. 2003), this implies that less than 1% of H_2 is heated to more than 300 K. In comparison with the starbursts observed by Rigopoulou et al. (2002), this fraction is low. However, in the latter objects, the contribution of photodissociation regions to the heating of H_2 is likely dominant, and the volume fraction of the molecular gas directly exposed to FUV radiation is probably much larger than in NGC 1377.

9. Alternative hypotheses to a nascent starburst

Different scenarios to account for the synchrotron deficiency (starburst deficient in high-mass stars, abnormally weak or strong magnetic field, dominant inverse Compton losses, extremely high electron opacity) were discussed at length by Roussel et al. (2003), and it was concluded that the most likely explanation involved a very young starburst. The possibility that a substantial population of relativistic electrons exists, but decays at a higher rate than the type-II supernova rate, in the hypothesis of inverse Compton losses dominating synchrotron losses, is not formally ruled out, but seems in conflict with other properties of the starburst. In particular, we did not detect the [FeII] line at $1.644 \mu\text{m}$, which is a quantitative tracer of shocks in supernova remnants (Vanzi & Rieke 1997), where cosmic ray electrons are accelerated ; the line flux ratio of [FeII] to H_2 at $2.122 \mu\text{m}$ is below 0.1 in NGC 1377, whereas it is above 2 for the mature starburst in NGC 1022, which we chose as a comparison galaxy (see also Larkin et al. (1998) and Dale et al. (2004)). Reconciling these ratios by invoking differential extinction effects (and assuming cospatial emission) would imply $\tau_V > 50$, whereas we have derived $\tau_V < 17$ for H_2 (Section 8). The massive stars in NGC 1377 are thus unlikely to have reached the supernova stage. In addition, it is hardly conceivable that a starburst older than 5 Myr would still be completely embedded, despite the effects of winds from massive stars and supernova shock waves on the interstellar medium. On the other hand, most cosmic rays generated by past star formation episodes would presumably have propagated over large distances and be located outside the current starburst region, which is very compact, and thus outside of reach of the intense radiation field of the starburst. Their absence is thus more plausibly due to NGC 1377 being previously quiescent for a long period, than to their suppression by inverse Compton losses. Finally, we know of some ultraluminous galaxies, studied by Condon et al. (1991), that host very compact starbursts with radiation fields at least as intense as in NGC 1377 ; yet, they are bright synchrotron emitters, which implies that their magnetic field has been amplified to

the degree necessary to balance inverse Compton losses by synchrotron losses. It is unclear why magnetic field amplification would be inhibited in NGC 1377. In summary, the issue of inverse Compton losses is not settled by the present data, but we favor the hypothesis of a nascent starburst as much more likely.

Simple energetics arguments also led Roussel et al. (2003) to conclude that it would be exceedingly difficult to account for the observed properties of NGC 1377 by accretion onto a massive black hole. An upper limit on the mass of a black hole at the center of NGC 1377, of the order of $2 \times 10^5 M_\odot$, is derived consistently both from the lack of radio continuum emission (using an empirical relation between the minimum radio power emitted and the black hole mass of radio-quiet active nuclei) and from the narrow velocity profile of the H₂ 2.12 μm line (assuming virial equilibrium). In the unrealistic assumption that the efficiency of dust heating by the accretion power be 100%, this power would still have to be above the Eddington limit for a black hole of such a mass, to account for the observed infrared luminosity. In addition, substantial free-free emission would be observed, because a large fraction of the bolometric luminosity of active nuclei is ionizing ; the expected flux, at wavelengths short enough that thermal opacity is negligible, is well above the observational upper limit. A new element is brought by the Spitzer data to constrain the nature of the power source. The fact that no high-excitation lines are detected makes the hypothesis of non-stellar activity all the more difficult. In particular, since the [NeII] line is detected, the undetected [NeIII] line, affected by almost the same extinction and having a similar critical density, sets a meaningful constraint on the radiation hardness. Based on the results of Sturm et al. (2002), pure Seyfert nuclei (i.e. minimally contaminated by star formation) have $F_{\text{[NeIII]}}/F_{\text{[NeII]}}$ ratios between 1 and 3. This line flux ratio is lower than 0.5 in NGC 1377. We conclude that non-stellar activity is very unlikely to be responsible for the infrared power of NGC 1377.

10. Summary and discussion

NGC 1377 first attracted our attention as being extremely deficient in radio continuum emission, with respect to its infrared brightness. Its dust is also heated to very high temperatures, which implies an intense radiation field. The lack of synchrotron emission points to the galaxy being previously quiescent for at least 100 Myr (which is corroborated by optical spectral synthesis in Section 4), and the current star-forming episode being younger than the lifetime of type-II supernova progenitors (Roussel et al. 2003). Its far-infrared (40–120 μm) luminosity is about $4 \times 10^9 L_\odot$, and the bolometric luminosity of the starburst is of the order of $1.1 \times 10^{10} L_\odot$. This corresponds to a starburst with a $1.6 \times 10^7 M_\odot$ stellar mass,

assuming an age of 1 Myr and a Salpeter initial mass function between 0.1 and $120 M_{\odot}$ (or $6 \times 10^6 M_{\odot}$ for a lower mass cutoff of $1 M_{\odot}$), and about 3×10^4 O stars. The global cold molecular gas properties are similar to those of starbursts, with subthermal excitation and a high far-infrared to CO flux ratio. The molecular gas mass, $\sim 2 \times 10^8 M_{\odot}$, is only 10 to 30 times higher than the estimated starburst mass, which implies an extremely short gas exhaustion timescale for NGC 1377. The size of the infrared source is of the order of 100 pc or smaller, and the new observations reveal that the optical depth in the amorphous silicate absorption bands is one of the highest observed in extragalactic systems: the apparent optical depth at $10 \mu\text{m}$, of the order of 4, is very similar to that of IRAS 08572+3915, the most deeply obscured object in the sample of infrared-luminous galaxies of Spoon et al. (2006a). It should be noted that the modelled optical depth of NGC 1377 is about five times higher than the apparent depth. A few absorption bands from dense and warm molecular gas are also present, although very faint.

The new data confirm that NGC 1377 has the characteristics of an extremely young, totally opaque nuclear starburst. It is in such an early phase of this starburst that the only tracer of HII regions yet detected is a very weak [NeII] line. Due to a combination of two effects, suppression of the ionizing photons by dust and high optical depth in the mid-infrared, the [NeII] line probes only $\sim 0.8\%$ of the intrinsic ionizing photon flux of the starburst. The growth of the HII regions is probably still inhibited by the pressure of the dense interstellar medium, and a large fraction of the massive stars must be still embedded in their parent molecular cloud. In order to reconcile the presence of very massive stars in nuclear starbursts with their nebular line ratios typically indicating low excitation (Thornley et al. 2000), Rigby & Rieke (2004) proposed that in such environments, high pressure causes massive stars to spend a large fraction of their lifetime in ultracompact HII regions, where the production of nebular lines is quelled. NGC 1377 could represent an extreme example of this phenomenon. Galactic systems where the dust competes so efficiently with gas for absorption of the stellar radiation are extremely rare.

If we try to understand the starburst in NGC 1377 as a scaled-up version of stellar-size objects (as a mental picture only), the class of Becklin-Neugebauer (BN) objects may represent the closest analogs suited to that purpose. BN objects are at the transition between massive protostars and pre-main-sequence stars exciting ultracompact HII regions, after the intense accretion phase has stopped, but before the radiation pressure has balanced the interstellar medium pressure (Henning & Gürtler 1986). The emergent infrared radiation is strongly self-absorbed like in NGC 1377, and molecular hydrogen is excited by shocks, caused by the interaction of stellar outflows with the molecular envelope. It is unclear whether the same H₂ heating mechanism applies to NGC 1377. Shocks could be caused by the collective outflows and winds of massive protostars and young stars ; or they could be caused by a

merger event, provided the disturbances revealed by optical color maps (Sect. 3) may be interpreted in this fashion. The optical forbidden line spectrum supports the existence of shocks also in the foreground of the region of activity (Sect. 4).

The central neutral density inferred from a radiative transfer model is of the order of 10^4 hydrogen nuclei cm^{-3} , which is not greater than typical densities of giant molecular clouds. The estimated starburst mass (see above) is also very similar to the mass of the super star cluster coincident with the brightest mid-infrared source in the Antennae galaxies (Gilbert et al. 2000), although the latter cluster is more evolved, since it is associated with bright HII and photodissociation regions. In view of these results, we are not able to determine whether the activity in NGC 1377 arises from the formation of a single cluster, or from several isolated pockets. We had been led to the latter hypothesis by the fact that the molecular gas could be unstable with respect to gravitational instabilities (Roussel et al. 2003), so that star formation could be triggered almost instantaneously at several locations. The data are however compatible with the formation of a single stellar cluster in the nucleus. This question should be more easily addressed for more luminous objects.

At the other end of the mass and luminosity scale, the infrared spectrum of NGC 1377 is indeed strikingly similar to those of some deeply obscured infrared-luminous galaxies (Fig. 13). NGC 4418 and IRAS 08572+3915 for instance (Spoon et al. 2001, 2006a) share the main spectral characteristics of NGC 1377. In addition, these luminous galaxies are part of a statistical sample of nascent starbursts that we have selected by their deviation from the infrared-radio correlation and their hot dust. Forthcoming papers will present and discuss the infrared-radio properties and molecular gas content of this sample, based on observations with Spitzer, the VLA array and the IRAM 30 m telescope. The characteristics of these galaxies will be contrasted with those of NGC 1377, serving as an archetype of the nascent starburst class. Their diverse radio continuum properties suggest that they should sample well young starbursts at various stages of development (Roussel et al. 2005). It will be one of our aims to sketch an empirical evolutionary sequence from dust-bounded nascent starbursts such as NGC 1377 to mature starbursts such as M 82.

We have previously derived a rate of occurrence of the nascent starburst phenomenon of $\sim 16\%$ among galaxies whose flux density distribution peaks at $60 \mu\text{m}$ (Roussel et al. 2003). This rate is not in conflict with the expected timescales of star formation. Nascent starbursts, as we have defined them, must fulfill two conditions: their current star formation episode must be younger than 5 Myr, and they must previously have been quiescent for ~ 100 Myr. If we note the typical duration of compact starbursts $t \times 5$ Myr, where t is probably not much larger than unity, then the fraction of starbursts occurring in isolated mode (as opposed to recurrent mode) would be $0.16 \times t$.

Starburst tracks currently do not incorporate the pre-HII nucleus phase. Likewise, the sets of galactic templates used to interpret the infrared counts in deep surveys do not include objects such as NGC 1377. Since even small changes in the assumed spectrum of aromatic bands in the mid-infrared yield important differences in the interpretation of the counts, as emphasized by Smith et al. (2006), the consequences of the existence of luminous galaxies sharing the properties of NGC 1377 cannot be neglected. This is illustrated by Figure 14, showing the large differences in the redshift-luminosity curve for the $24\mu\text{m}$ MIPS filter, according to the assumed mid-infrared spectral energy distribution: the curve obtained for NGC 1377 is vastly different from those of popular starburst templates. The nascent starbursts (selected by their deficiency in radio continuum emission, with respect to the infrared) are rare objects, in agreement with the brevity of their evolutionary phase. However, they represent a non-negligible fraction of galaxies with $F_{60\mu\text{m}} > F_{100\mu\text{m}}$, whose frequency may be much higher at earlier epochs, as suggested by the results of Chapman et al. (2004).

We wish to thank Marc Sauvage for fruitful discussions, Mark Wolfire for tirelessly running photodissociation region models to help interpret the data, and Nancy Silbermann for the timely scheduling of the Spitzer IRS observations. Support for this work, part of the Spitzer Space Telescope Legacy Science Program, was provided by NASA through an award issued by the Jet Propulsion Laboratory, California Institute of Technology under NASA contract 1407.

REFERENCES

Asplund, M., Grevesse, N., Sauval, A.J., Allende Prieto, C., & Kiselman, D. 2004, A&A, 417, 751

Baldwin, J.A., Phillips, M.M., & Terlevich, R. 1981, PASP, 93, 5

Beck, R., & Golla, G. 1988, A&A, 191, L9

Beck, S.C, Turner, J.L., Langland-Shula, L.E., et al. 2002, AJ, 124, 2516

Beck, S.C, Turner, J.L., & Kovo, O. 2000, ApJ, 120, 244

Bianchi, S., Davies, J.I., & Alton P.B. 1999, A&A, 344, L1

Bruzual, G., & Charlot, S. 2003, MNRAS, 344, 1000

Butler, K., & Zeippen, C.J. 1994, A&AS, 108, 1

Calzetti, D. 1997, AJ, 113, 162

Chapman, S.C., Smail, I., Blain, A.W., & Ivison, R.J. 2004, ApJ, 614, 671

Chiar, J.E., Tielens, A.G., Whittet, D.C., et al. 2000, ApJ, 537, 749

Condon, J.J. 1992, ARA&A, 30, 575

Condon, J.J., Huang, Z.P., Yin, Q.F., & Thuan T.X. 1991, ApJ, 378, 65

Dale, D.A., Roussel, H., Contursi, A., et al. 2004, ApJ, 601, 813

Decin, L., Morris, P.W., Appleton, P.N., Charmandaris, V., Armus, L., & Houck, J.R. 2004, ApJS, 154, 408

Dopita, M.A. 1977, ApJS, 33, 437

Draine, B.T., & Lee, H.M. 1984, ApJ, 285, 89

Dufton, P.L., & Kingston, A.E. 1991, MNRAS, 248, 827

Fazio, G., Hora, J.L., Allen, L.E., et al. 2004, ApJS, 154, 10

Galavis, M.E., Mendoza, C., & Zeippen, C.J. 1995, A&AS, 111, 347

Gilbert, A.M., Graham, J.R., McLean, I.S., et al. 2000, ApJ, 533, L57

Grevesse, N., & Sauval, A.J. 1998, SSRv, 85, 161

Habing, H.J., & Israel, F.P. 1979, ARA&A, 17, 345

Heisler, C.A., & Vader, J.P. 1994, AJ, 107, 35

Helou, G., Soifer, B.T., & Rowan-Robinson, M. 1985, ApJ, 298, L7

Helou, G., & Bicay, M.D. 1993, ApJ, 415, 93

Henning, T., & Gürtler, J. 1986, Ap&SS, 128, 199

Herbst, T.M., Beckwith, S.V., Glindemann, A., Tacconi-Garman, L.E., Kroker, H., & Krabbe, A. 1996, AJ, 111, 2403

Hollenbach, D.J., & Tielens, A.G. 1997, ARA&A, 35, 179

Houck, J.R., Roellig, T.L., van Cleve, J., et al. 2004a, ApJS, 154, 18

Houck, J.R., Charmandaris, V., Brandl, B.R., et al. 2004b, ApJS, 154, 211

Hunt, L., Bianchi, S., & Maiolino, R. 2005, A&A, 434, 849

de Jong, T., Klein, U., Wielebinski, R., & Wunderlich E. 1985, A&A, 147, L6

Kaufman, M.J., Wolfire, M.G., & Hollenbach, D.J. 2006, submitted to ApJ

Kennicutt, R.C., et al. 2003, PASP 115, 928

Van Kerckhoven, C., Hony, S., Peeters, E., et al. 2000, A&A, 357, 1013

Kim, D.C., Sanders, D.B., Veilleux, S., Mazzarella, J.M., & Soifer B.T. 1995, ApJS, 98, 129

Kobulnicky, H.A., & Johnson, K.E. 1999, ApJ, 527, 154

Koike, C., Shibai, H., & Tuchiyama, A. 1993, MNRAS, 264, 654

Laor, A., & Draine, B.T. 1993, ApJ, 402, 441

Larkin, J.E., Armus, L., Knop, R.A., Soifer, B.T., & Matthews, K. 1998, ApJS, 114, 59

Laureijs, R.J., Watson, D., Metcalfe, L., et al. 2000, A&A, 359, 900

Leitherer, C., Schaerer, D., Goldader, J.D., et al. 1999, ApJS, 123, 3

Li, A., & Draine, B.T. 2001, ApJ, 554, 778

Lisenfeld, U., Völk, H.J., & Xu C. 1996, A&A, 314, 745

Lonsdale-Persson, C.J., & Helou, G. 1987, ApJ, 314, 513

Malhotra, S., Kaufman, M.J., Hollenbach, D.J., et al. 2001, ApJ, 561, 766

Mathis, J.S., Rumpl, W., & Nordsieck, K.H. 1977, ApJ, 217, 425

Molster, F.J., Waters, L.B., & Tielens, A.G. 2002, A&A, 382, 222

Moneti, A., Stolovy, S., Blommaert, J.A., Figer, D.F., & Najarro, F. 2001, A&A, 366, 106

Moustakas, J., & Kennicutt, R.C. 2006, ApJ, in press

Nenkova, M., Ivezić, Z., & Elitzur, M. 2000, ASPC, 196, 77

Niklas, S., & Beck, R. 1997, A&A, 320, 54

Ossenkopff, V., Henning, T., & Mathis, J.S. 1992, A&A, 261, 567

Peeters, E., Allamandola, L.J., Bauschlicher, C.W., Hudgins, D.M., Sandford, S.A., & Tielens, A.G. 2004, *ApJ*, 604, 252

Peeters, E., Hony, S., Van Kerckhoven, C., et al. 2002, *A&A*, 390, 1089

Plante, S., & Sauvage, M. 2002, *AJ*, 124, 1995

Rieke, G., Young, E.T., Engelbracht, C.W., et al. 2004, *ApJS*, 154, 25

Rigby, J.R., & Rieke, G.H. 2004, *ApJ*, 606, 237

Rigopoulou, D., et al. 2002, *A&A*, 389, 374

Roussel, H., Helou, G., Condon, J., & Beck, R. 2005, *Ap&SS*, 329, 223

Roussel, H., Helou, G., Beck, R., Condon, J.J., Bosma, A., Matthews, K., & Jarrett, T.H. 2003, *ApJ*, 593, 733

Salpeter, E.E. 1955, *ApJ*, 121, 161

Saraph, H.E., & Tully, J.A. 1994, *A&AS*, 107, 29

Sauvage, M., & Thuan, T.X. 1992, *ApJ*, 396, L69

Smith, J.D., et al. 2006, submitted to *ApJ*

Smith, J.D., Dale, D.A., Armus, L., et al. 2004, *ApJS*, 154, 199

Sodroski, T.J., Bennett, C., Boggess, N., et al. 1994, *ApJ*, 428, 638

Spoon, H.W., Keane, J.V., Cami, J., et al. 2006b, *IAU Symposium* 231

Spoon, H.W., Tielens, A.G., Armus, L., et al. 2006a, *ApJ*, 638, 759

Spoon, H.W., Armus, L., Cami, J., et al. 2004, *ApJS*, 154, 184

Spoon, H.W., Keane, J.V., Tielens, A.G., Lutz, D., & Moorwood, A.F. 2001, *A&A*, 365, L353

Storey, P.J., & Hummer, D.G. 1995, *MNRAS*, 272, 41

Sturm, E., Lutz, D., Verma, A., et al. 2002, *A&A*, 393, 821

Sturm, E., Lutz, D., Tran, D., et al. 2000, *A&A*, 358, 481

Tarchi, A., Neininger, N., Greve, A., et al. 2000, *A&A*, 358, 95

Thornley, M.D., Förster Schreiber, N.M., Lutz, D., et al. 2000, *ApJ*, 539, 641

Turner, J.L., Ho, P.T., & Beck, S.C. 1998, *AJ*, 116, 1212

Turner, J., Kirby-Docken, K., & Dalgarno, A. 1977, *ApJS*, 35, 281

Vanzi, L., & Rieke, G.H. 1997, *ApJ*, 479, 694

de Vaucouleurs, G., de Vaucouleurs, A., Corwin, H.G., Buta, R.J., Paturel, G., & Fouque, P. 1991, *Third Reference Catalogue of Bright Galaxies*, ed. Springer-Verlag

Weingartner, J.C., & Draine, B.T. 2001, *ApJ*, 548, 296

Werner, M.W., Uchida, K.I., Sellgren, K., et al. 2004, *ApJS*, 154, 309

Willmer, C.N., Focardi, P., da Costa, L.N., & Pellegrini, P.S. 1989, *AJ*, 98, 1531

Worthey, G., Faber, S.M., Jesús González, J., & Burstein, D. 1994, *ApJS*, 94, 687

Zubko, V., Dwek, E., & Arendt, R.G. 2004, *ApJS*, 152, 211

Table 1. Flux densities of NGC 1377 in the Spitzer bands (this study ; see text) and in the ISO and IRAS bands (Roussel et al. 2003). The total photometric uncertainty for the Spitzer measurements is of the order of 10% in the IRAC bands, 5% at $24\text{ }\mu\text{m}$, 10% at $71\text{ }\mu\text{m}$ and 15% at $156\text{ }\mu\text{m}$; for the ISOCAM measurements, $\sim 20\%$; and for the IRAS measurements, 10% at 12 and $25\text{ }\mu\text{m}$ and 15% at 60 and $100\text{ }\mu\text{m}$ (IRAS Explanatory Supplement).

band	nuclear flux (Jy)	total flux (Jy)
$3.6\text{ }\mu\text{m}$ (IRAC)	0.0199 ^a	0.0591
$4.5\text{ }\mu\text{m}$ (IRAC)	0.0520	0.0817
$5.7\text{ }\mu\text{m}$ (IRAC)	0.2715	= nuclear
$6.7\text{ }\mu\text{m}$ (ISOCAM)		$0.366 - 0.391^{\text{b}}$
$7.9\text{ }\mu\text{m}$ (IRAC)	0.4105	= nuclear
$12\text{ }\mu\text{m}$ (IRAS)		0.43
$14.3\text{ }\mu\text{m}$ (ISOCAM)		$0.705 - 0.721^{\text{b}}$
$24\text{ }\mu\text{m}$ (MIPS)		1.740
$25\text{ }\mu\text{m}$ (IRAS)		1.83
$60\text{ }\mu\text{m}$ (IRAS)		7.01
$71\text{ }\mu\text{m}$ (MIPS)		5.64 ^c
$100\text{ }\mu\text{m}$ (IRAS)		5.97
$156\text{ }\mu\text{m}$ (MIPS)		3.19 ^c

^aIf we try to decompose the surface brightness profile in the $3.6\text{ }\mu\text{m}$ band to estimate the central brightness of the disk, and adjust a point spread function to the residual central brightness above this level, we obtain an estimate of 0.0162 Jy for the nuclear flux, i.e. 10% lower.

^bThe two flux values for each ISOCAM band correspond to measurements before and after correction for a slight saturation of the nuclear pixels.

^cThe MIPS 71 and $156\text{ }\mu\text{m}$ fluxes include the latest flux calibration adjustments (+11% and +6% respectively, from version S12 to version S13 of the Spitzer Science Center pipeline).

Table 2. Line fluxes and upper limits and critical densities of the forbidden lines^a. All lines were measured at high spectral resolution, except H₂ v=0 S(3) which is outside the wavelength coverage of the high-resolution modules. The uncertainties on the critical densities reflect a range of electronic temperature between 5×10^3 K and 10^4 K.

line	rest wavelength (μm)	spectral order	flux ($10^{-18} \text{ W m}^{-2}$)	critical density (cm^{-3})
H ₂ v=0 S(0)	28.219	LH 14	< 9.15	
H ₂ v=0 S(1)	17.035	SH 12	65.43 ± 2.94	
H ₂ v=0 S(2)	12.279	SH 17	39.14 ± 10.03	
H ₂ v=0 S(3)	9.665	SL 1	65.10 ± 7.64	
[SIII]	34.814	LH 11	< 11.93	$(1.5 \pm 0.3) \times 10^3$
[SIII]	33.480	LH 12	< 7.20	$(6.1 \pm 0.9) \times 10^3$
[SIII]	18.713	SH 11	< 2.00	$(2.0 \pm 0.3) \times 10^4$
[NeIII]	15.555	SH 13	< 8.97	$(2.4 \pm 0.4) \times 10^5$
[NeII]	12.814	SH 16	17.38 ± 2.13	$(6.0 \pm 1.0) \times 10^5$

^aThe critical densities are computed as: $N_{\text{crit}} = A / [C (T_e/1\text{K})^{-0.5} \Omega(T_e) g_u^{-1}]$, where A is the transition probability, taken in the NIST atomic spectra database (<http://physics.nist.gov/PhysRefData/ASD>), $C = 8.6287 \times 10^{-6} \text{ cm}^3 \text{ s}^{-1}$, and g_u is the statistical weight of the upper level. We used collision strengths from Galavis et al. (1995) for the [SIII] lines and Dufton & Kingston (1991) for the [SiII] line.

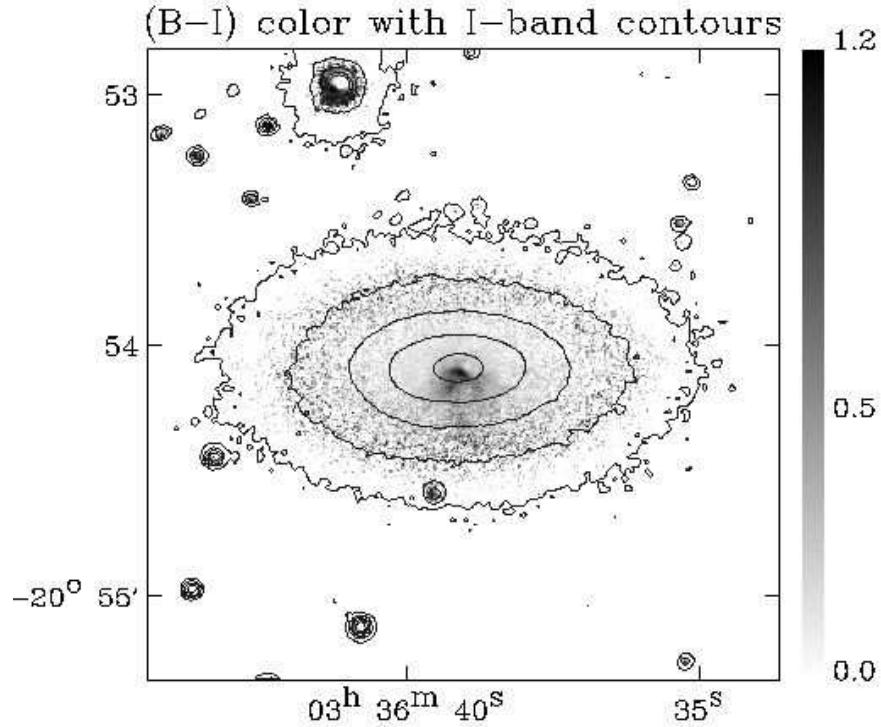


Fig. 1.— The (B-I) magnitude difference (with arbitrary zero-points because the maps are not flux-calibrated) is shown in grey scale, from 0 to 1.2 mag. The maximum color in the center of NGC 1377 is 0.1 mag higher than displayed here. Isophotes of the I-band image are superposed for the intensities $\sigma_I \times 3^n$, $n = 1$ to 5, where σ_I is the standard deviation of the sky brightness.

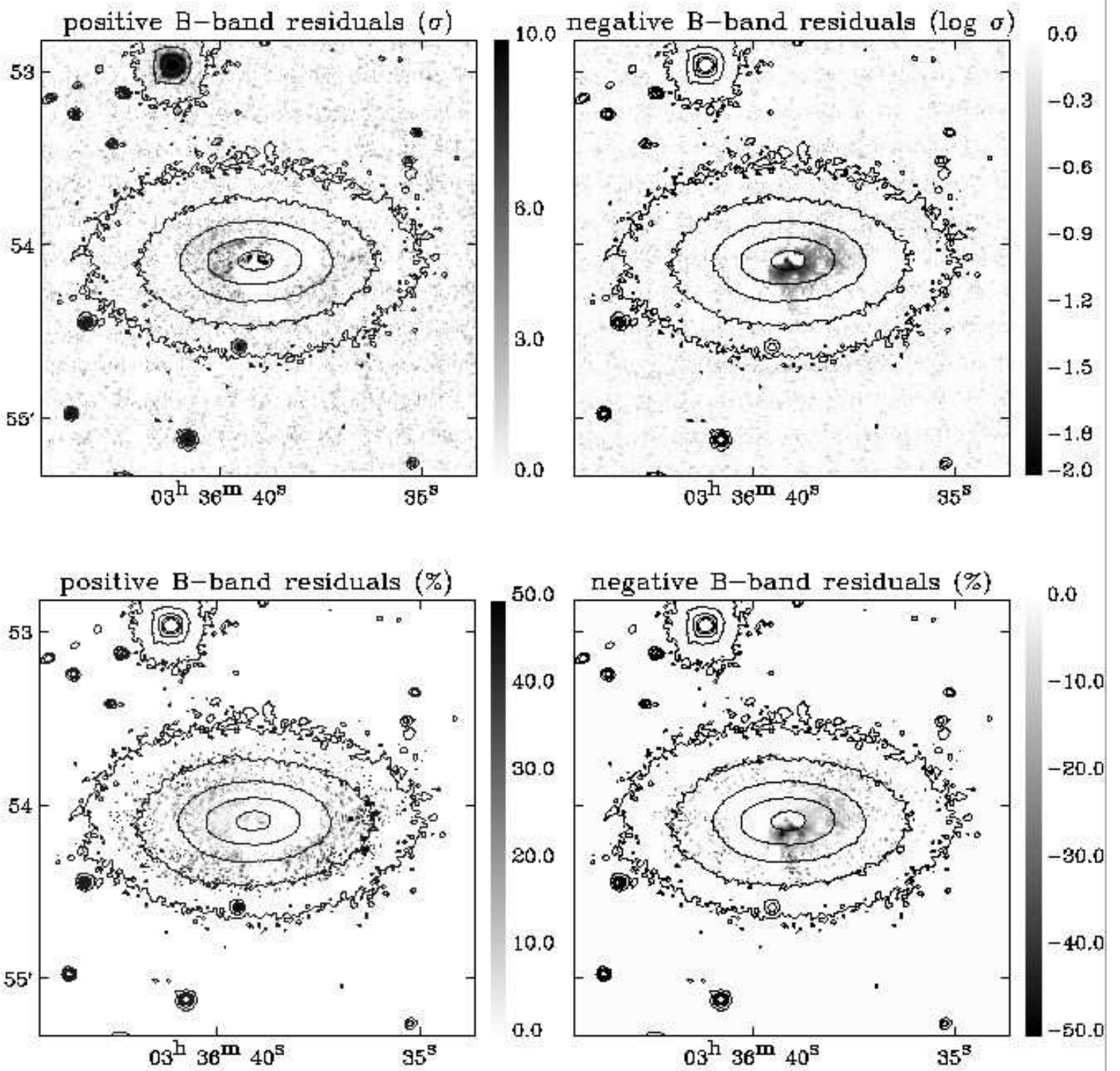


Fig. 2.—Residuals of the B-band image after subtraction of a smooth photometric model. To construct this model, radial brightness profiles were derived from small angular sections along the northern minor axis and along the eastern major axis, which appear undisturbed in the (B-I) color map. Then, the brightness distribution at any position angle θ was interpolated by affecting a weight $\cos^2\theta$ ($\sin^2\theta$) to the major (minor) axis profile. **Left:** positive residuals. **Right:** negative residuals. **Top:** in units of the standard deviation of the sky brightness (in logarithmic scale for the negative component). **Bottom:** as a percentage of the local model intensities. The contours are as in Figure 1.

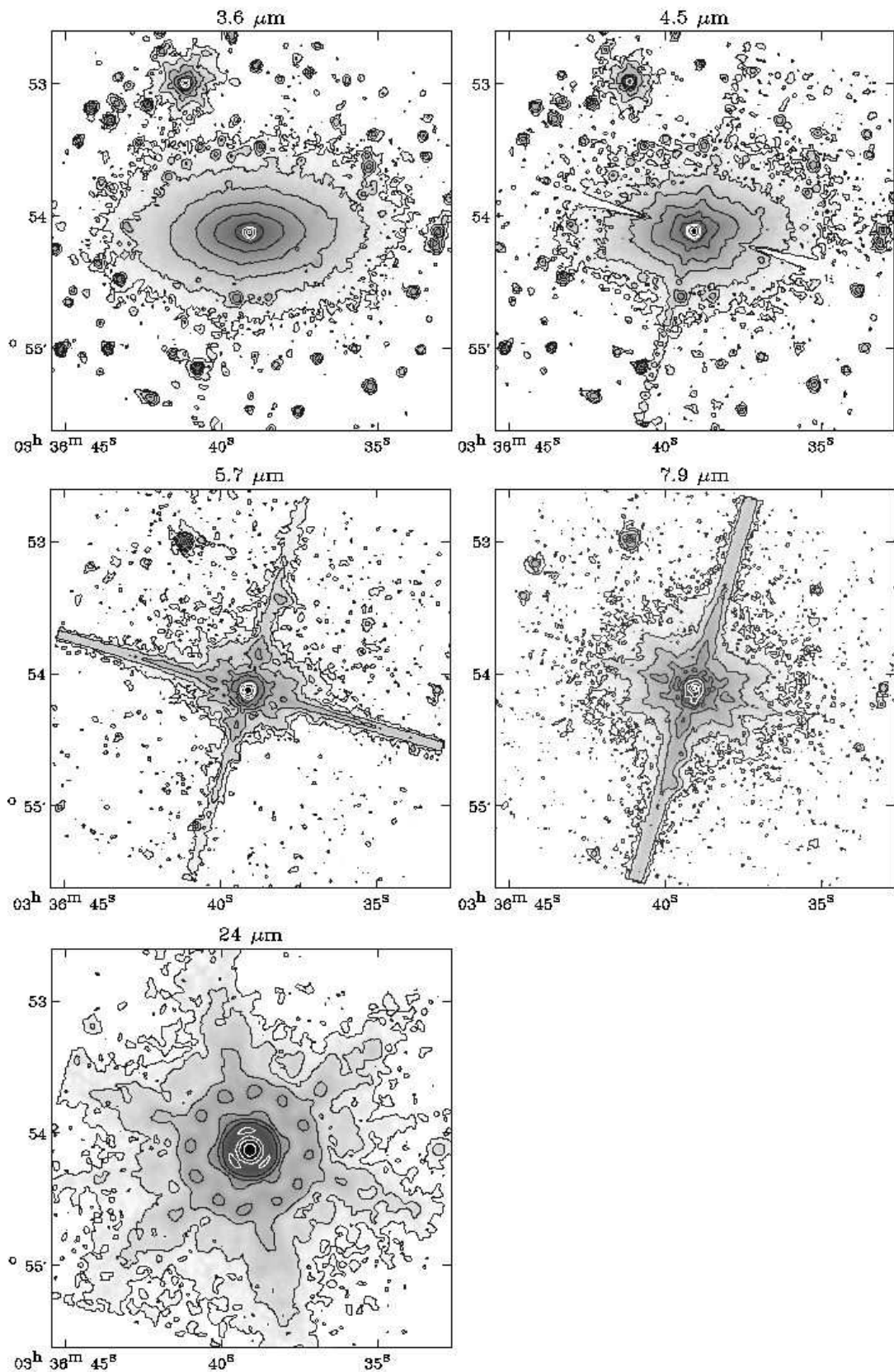


Fig. 3.— Infrared images of NGC 1377 in the four IRAC bands and in the 24 μm MIPS band. The contours are the isophotes $\sigma \times 3^n$, $n = 1$ to 9 for all bands except 7.9 μm , and $n = 1$ to 10 for 7.9 μm . The structure of the images is explained in the text (Sect. 3).

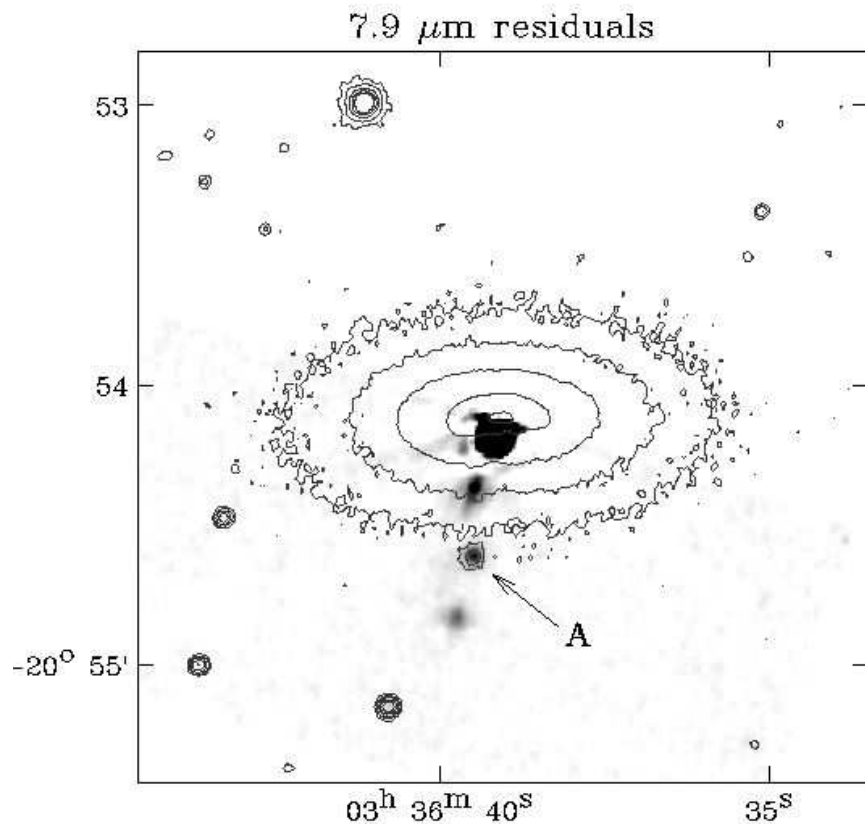


Fig. 4.— Residuals of the $7.9 \mu\text{m}$ image after subtraction of the mirrored northern half of the galaxy (see text). An intensity cut of 2 MJy/sr was applied. The brightest residuals have an intensity of $\sim 100 \text{ MJy/sr}$, and the peak brightness of the nucleus is about 2000 MJy/sr . The contours are the B-band isophotes of intensities $\sigma_B \times (1 + 3^n)$, $n = 1$ to 5. All the residuals are ghosts of the nucleus, except for the source labelled A.

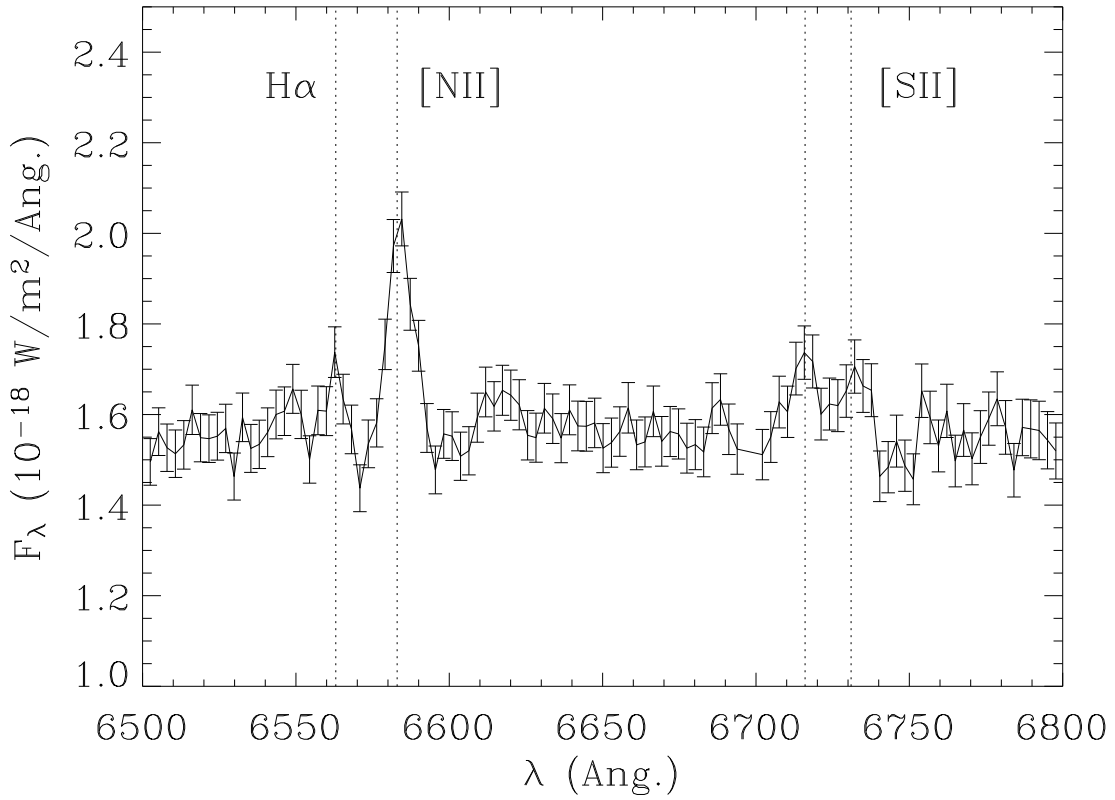


Fig. 5.— Rest-frame optical spectrum in the 6500–6800Å region, extracted in a $2.5'' \times 10''$ aperture centered on the nucleus. The vertical dotted lines indicate the wavelengths of the $\text{H}\alpha$, [NII] 6583Å, [SII] 6716Å and [SII] 6731Å lines.

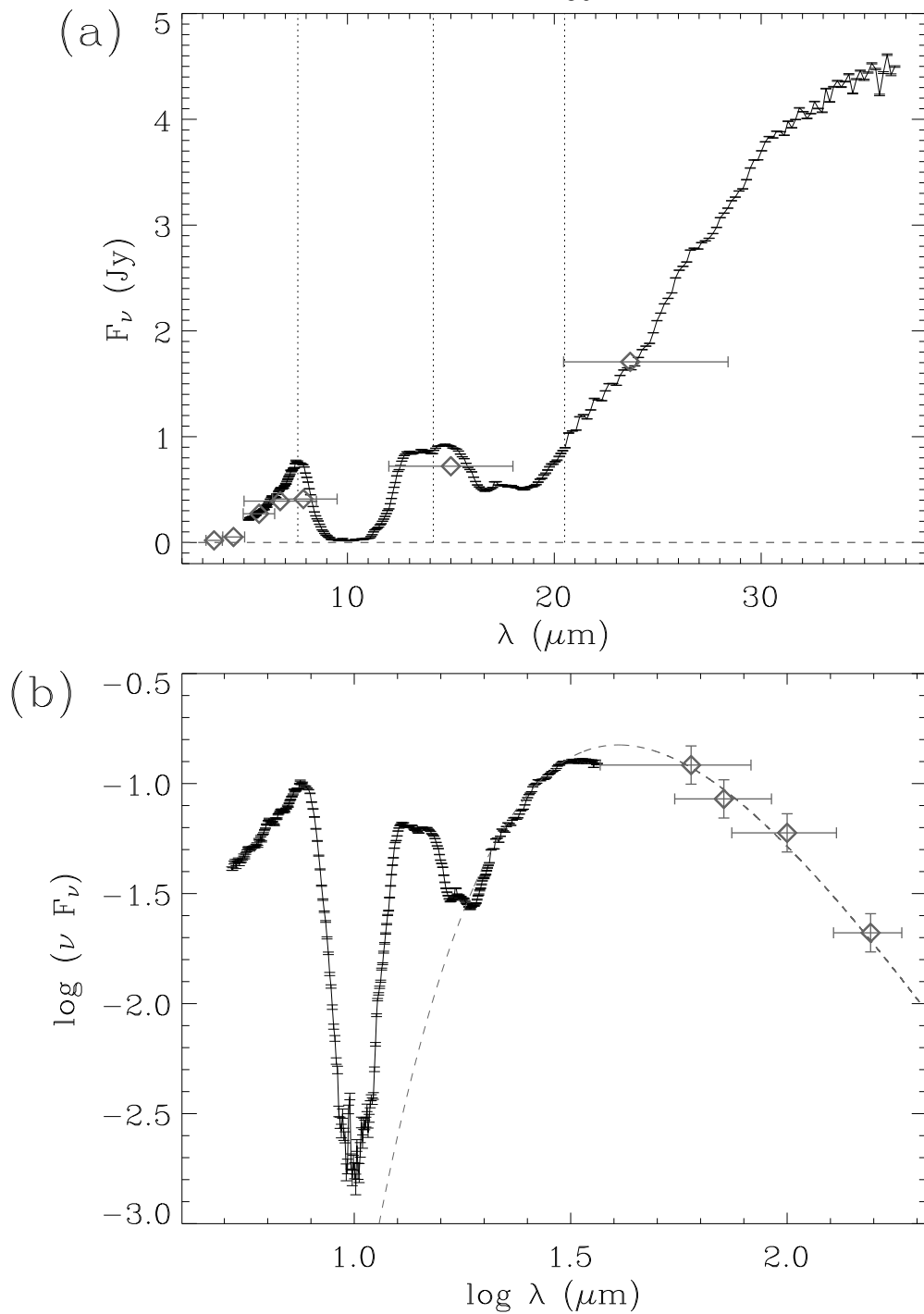


Fig. 6.— Spectral energy distribution of NGC 1377 between (a) 3 and $40\ \mu\text{m}$, in flux density units ; (b) 5 and $160\ \mu\text{m}$, in power units and logarithmic scale. Notice the very deep absorption bands from amorphous silicates at 10 and $18\ \mu\text{m}$. Broadband imaging photometry from IRAC, ISOCAM (6.75 and $15\ \mu\text{m}$), MIPS and IRAS (60 and $100\ \mu\text{m}$) is overplotted as grey diamond symbols with horizontal error bars representing the filter widths. In (a), the spectra from different orders (SL2, SL1, LL2 and LL1 in order of increasing wavelength) are separated by vertical dotted lines. In (b), the spectrum from a 90 K blackbody is overplotted as a grey dashed line.

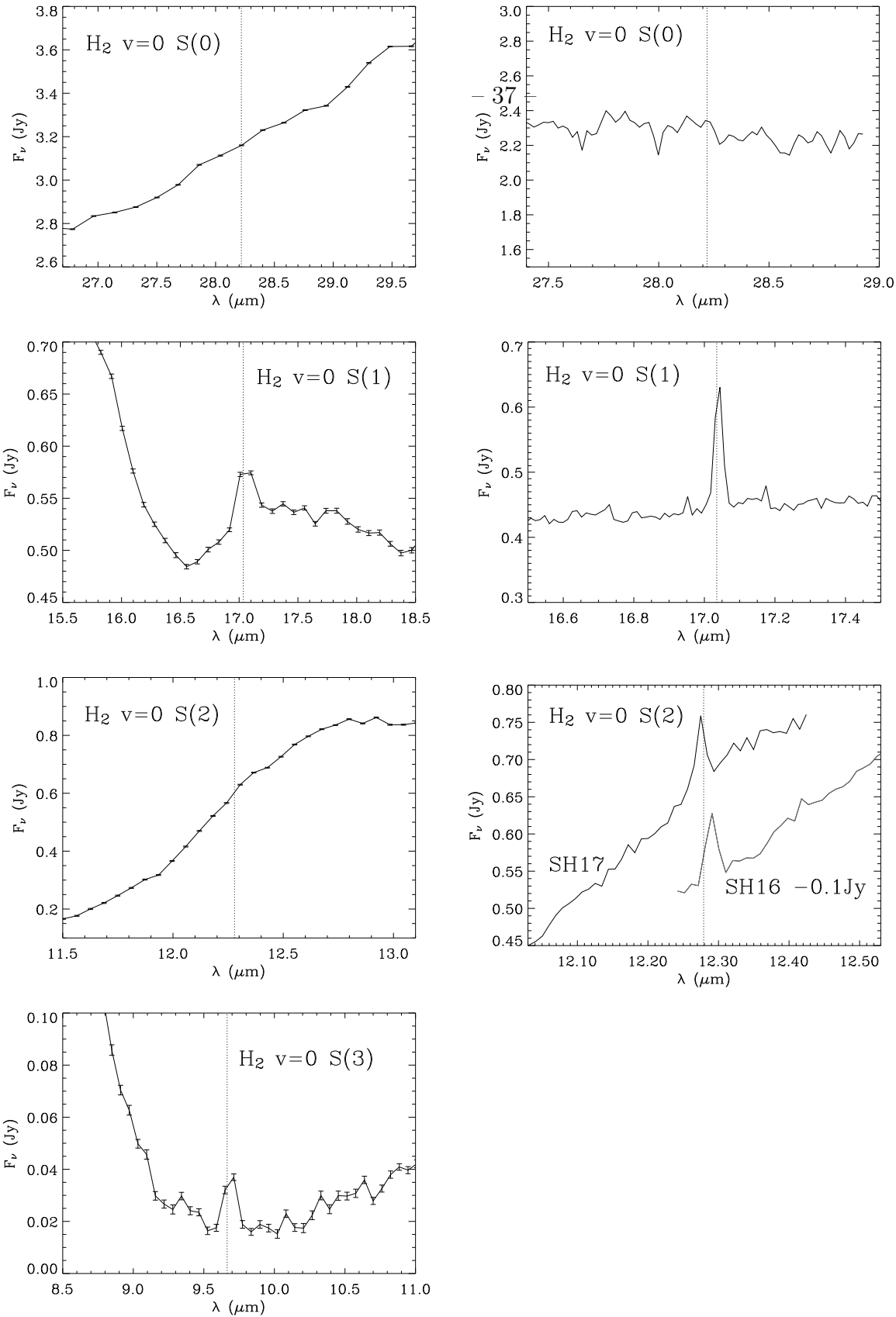


Fig. 7.— H_2 rotational lines in the mid-infrared spectrum of NGC 1377. **Left:** Rest-frame low-resolution spectra. **Right:** Rest-frame high-resolution spectra. The vertical dotted lines indicate the wavelengths of the transitions. The $12.29 \mu\text{m}$ transition is detected in two different spectral orders at high resolution ; the two spectra are overplotted, shifted in flux for clarity.

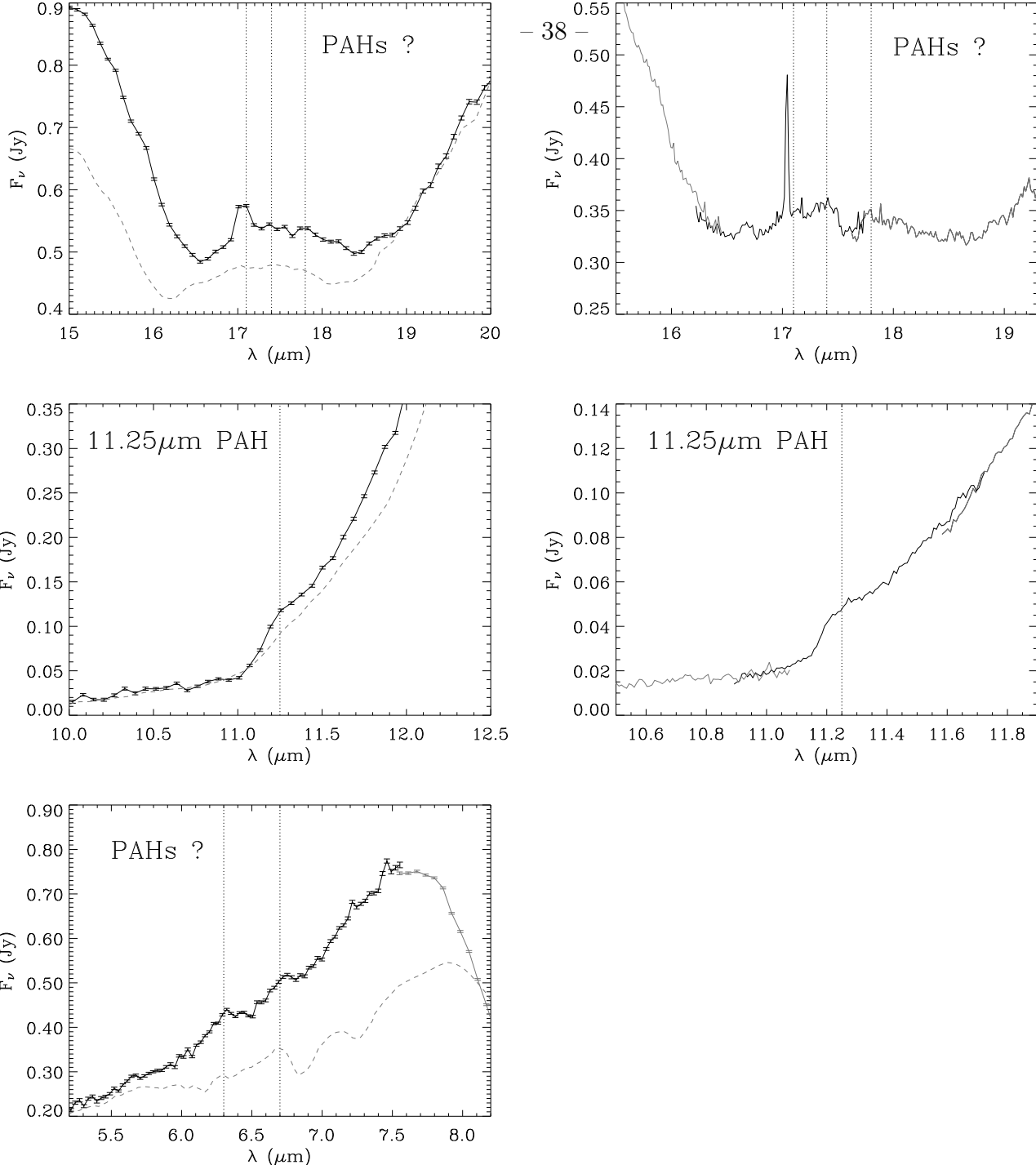


Fig. 8.— Tentative PAH detections in the mid-infrared spectrum of NGC 1377. **Left:** Rest-frame low-resolution spectra. **Right:** Rest-frame high-resolution spectra. Different colors are used for different spectral orders. Spectra in the SH module were extracted in smaller apertures to increase the signal to noise ratio (in the central 2×2 pixels for the $11.25 \mu\text{m}$ feature and 4×4 pixels for the $17 \mu\text{m}$ complex). For the $17 \mu\text{m}$ complex, the vertical dotted lines indicate the wavelengths of the 17.1 , 17.4 and $17.8 \mu\text{m}$ features. The prominent 17.03 H_2 line is not labelled here and shown separately in Figure 7. In the middle and bottom spectra, the vertical lines indicate the wavelengths of the $11.3 \mu\text{m}$, $6.3 \mu\text{m}$ and $6.7 \mu\text{m}$ features. For each low-resolution spectrum, the spectrum of IRAS 08572+3915, normalized to that of NGC 1377 at $36 \mu\text{m}$, is overplotted as a grey dashed line (see text).

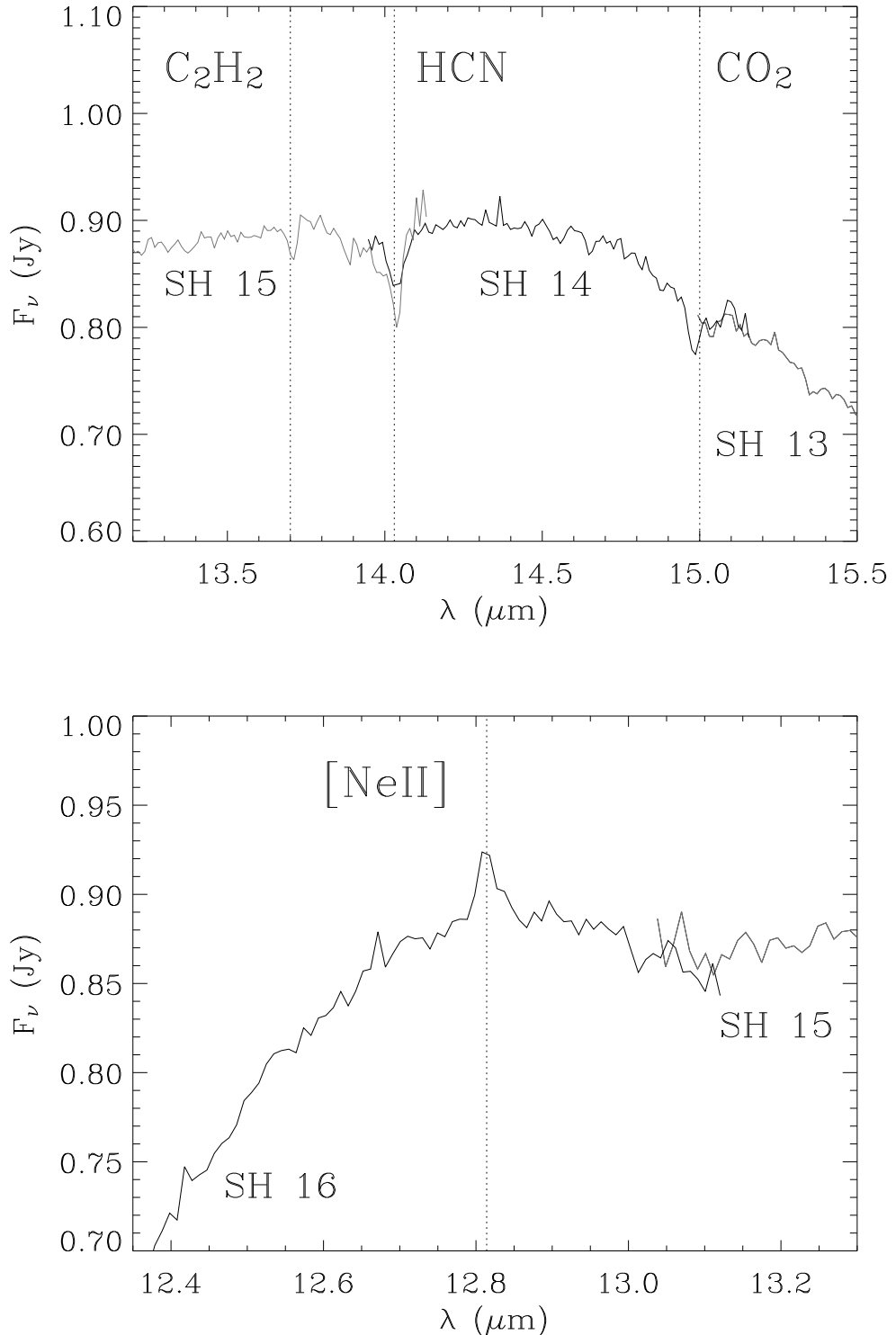


Fig. 9.— Rest-frame high-resolution spectra of faint molecular absorption features and of the [NeII] line. Different colors are used for different spectral orders. The vertical dotted lines indicate the wavelength of the features.

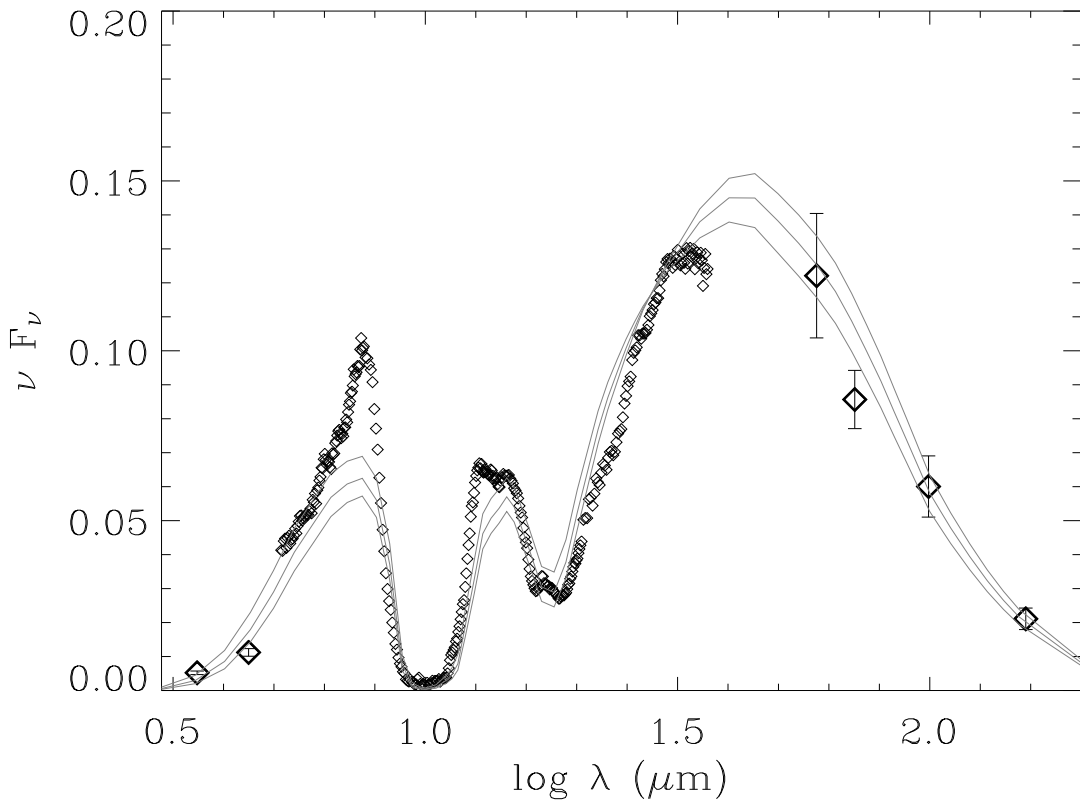


Fig. 10.— The fit to the infrared spectral energy distribution of NGC 1377 by the DUSTY model, with the parameters discussed in the text, is overplotted in grey, for $\tau_V = 75, 85$ and 95 . Broadband fluxes are shown as big diamonds with their error bars. Color corrections between 1.00 and 1.08 have been applied to the far-infrared fluxes ($60, 71, 100$ and $156 \mu\text{m}$) and corrections of 0.92 and 0.96 to the near-infrared fluxes (3.6 and $4.5 \mu\text{m}$).

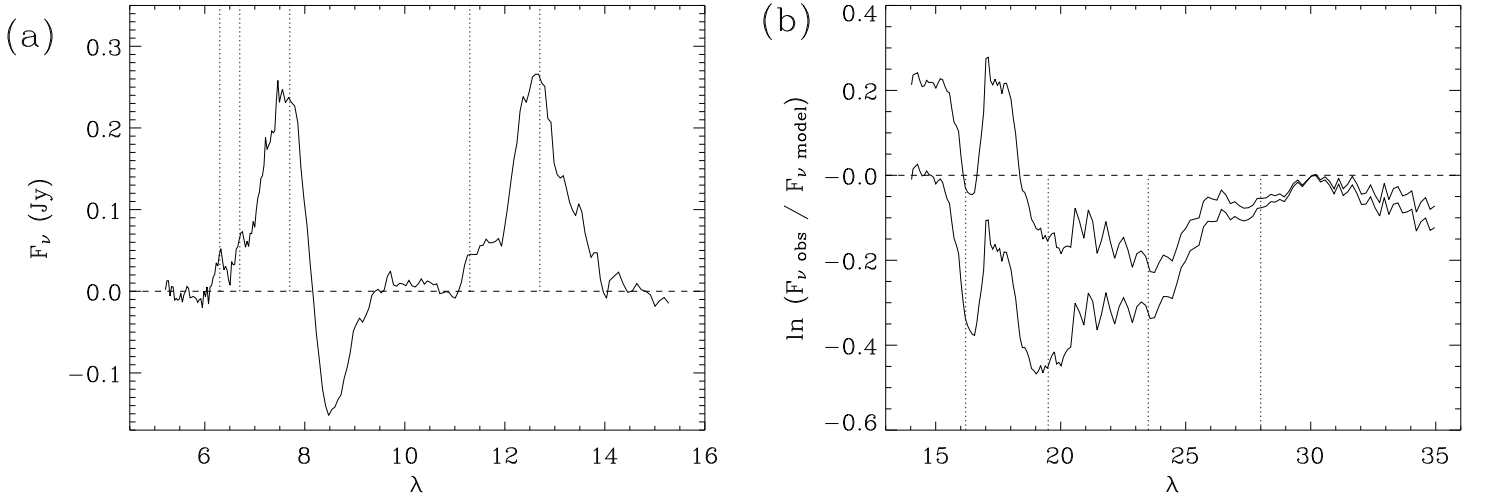


Fig. 11.— Residuals after subtraction or normalization by the DUSTY model. **(a)** Minimum residual emission in the 5–15 μm range (for $\tau_V = 75$). The peak wavelengths of the aromatic bands discussed in the text are shown by vertical dotted lines (at 6.3, 6.7, 7.7, 11.3 and 12.7 μm). We stress that due to modelling limitations, the 7.7 and 12.7 μm bands are very uncertain (see text). **(b)** Residuals in the 15–35 μm range shown for $\tau_V = 75$ (lower curve) and $\tau_V = 95$ (upper curve), in optical depth scale. The vertical lines indicate the positions of crystalline silicate features discussed by Spoon et al. (2006a) (at 16, 19.5, 23.5 and 28 μm). The effect of fringing is seen in observations with the LL1 module, particularly between 20.5 and 24 μm , and beyond 30 μm .

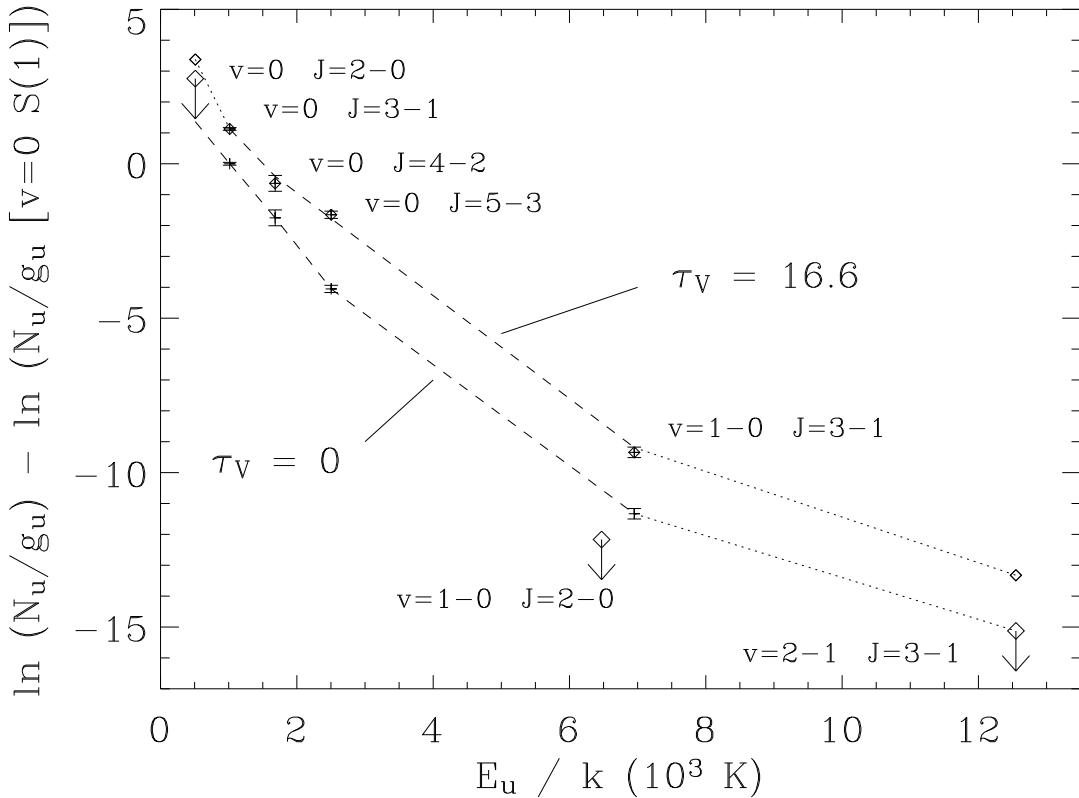


Fig. 12.— Excitation diagram for the observed rotational and rovibrational transitions of H₂. The abscissa is the temperature equivalent to the upper level energy of the transition, and the ordinate is the logarithm of the number of molecules in the upper level divided by the statistical weight, normalized by this ratio for the rotational S(1) line. The lower curve connects the data points uncorrected for extinction, and the upper curve corresponds to the maximum allowed extinction (see text), the normalization being done before the extinction correction. The $v=1-0$ S(0) upper limit, being inconsistent with the $v=1-0$ S(1) flux, was not considered, as it is probably underestimated.

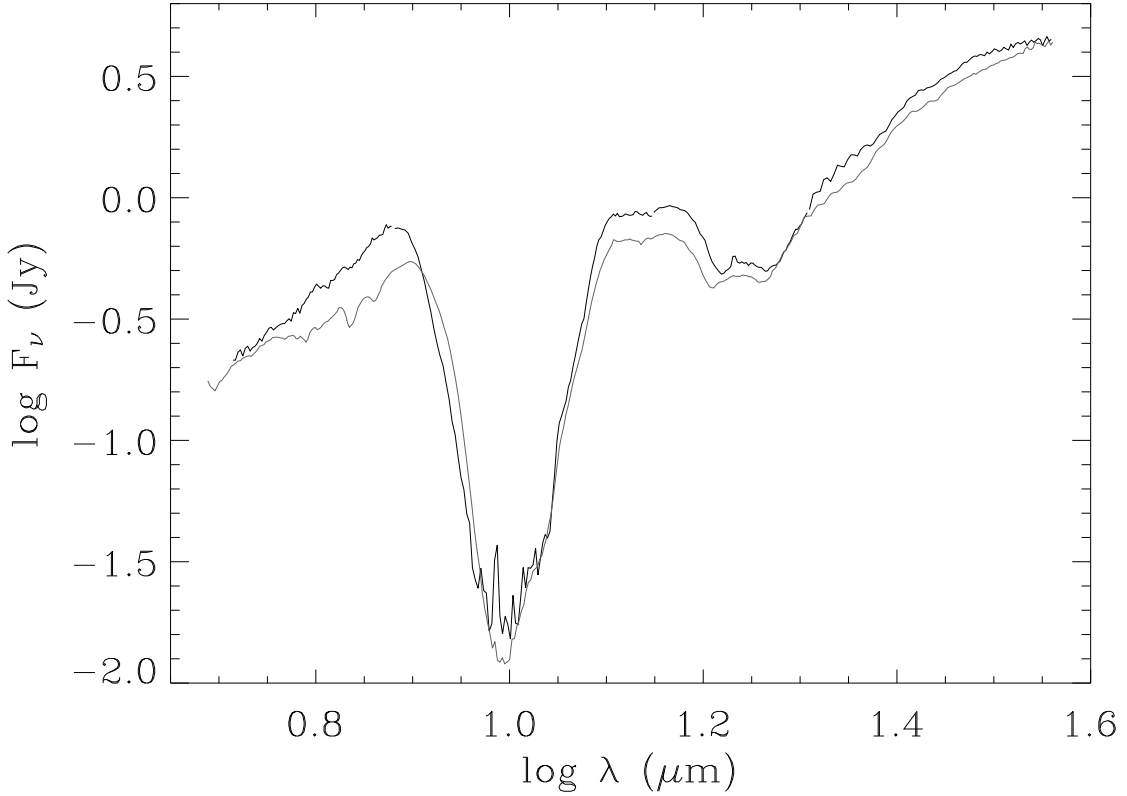


Fig. 13.— Comparison of the rest-frame mid-infrared spectra of NGC 1377 (this study) and IRAS 08572+3915 (Spoon et al. 2006a). The spectrum of NGC 1377 is shown in black. The spectrum of IRAS 08572+3915, normalized to that of NGC 1377 at the long-wavelength end of the LL1 module (36 μm), is shown in grey. The far-infrared (40–120 μm) luminosity of IRAS 08572+3915 is $\sim 5 \times 10^{11} L_\odot$, about 100 times the far-infrared luminosity of NGC 1377, and it has a slightly higher $F_{60\mu\text{m}}/F_{100\mu\text{m}}$ ratio of 1.4.

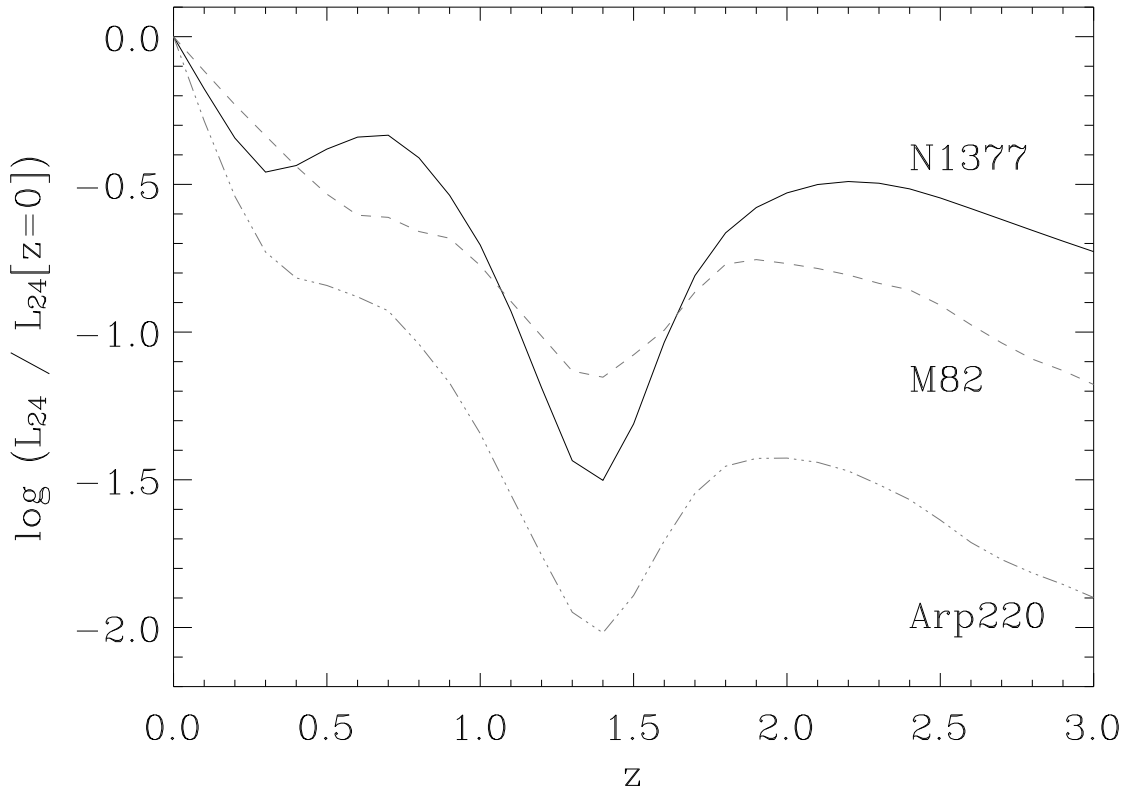


Fig. 14.— Evolution of the luminosity in the $24\mu\text{m}$ MIPS filter as a function of redshift, for three different mid-infrared spectral energy distributions: those of NGC 1377 (solid curve), M 82 (dashed curve) and Arp 220 (dot-dashed curve). M 82 and Arp 220 were chosen for this comparison because they are popular starburst templates.